NASA NIAC 2011 Supported Study

Meeting the Grand Challenge of Protecting Astronaut's Health: Electrostatic Active Space Radiation Shielding for Deep Space Missions

Final Report

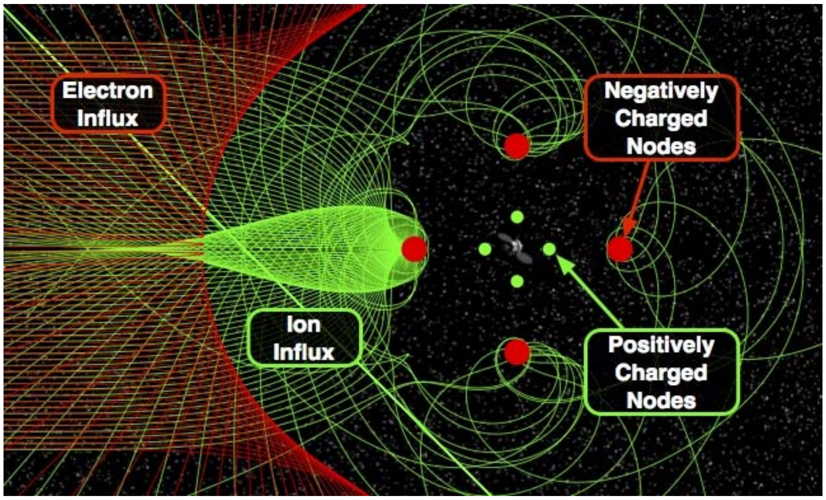

Principal Investigator:

Ram K. Tripathi[1]
NASA Langley Research Center, Hampton, VA 23681

---

[1] ram.k.tripathi@nasa.gov, (757) 864-1467

Abstract

This report describes the research completed during 2011 for the NASA Innovative Advanced Concepts (NIAC) project. The research is motivated by the desire to safely send humans in deep space missions and to keep radiation exposures within permitted limits. To this end current material shielding, developed for low earth orbit missions, is not a viable option due to payload and cost penalties. The active radiation shielding is the path forward for such missions. To achieve active space radiation shielding innovative large lightweight gossamer space structures are used. The goal is to deflect enough positive ions without attracting negatively charged plasma and to investigate if a charged Gossamer structure can perform charge deflections without significant structural instabilities occurring. In this study different innovative configurations are explored to design an optimum active shielding. In addition, to establish technological feasibility experiments are performed with up to 10kV of membrane charging, and an electron flux source with up to 5keV of energy and 5mA of current. While these charge flux energy levels are much less than those encountered in space, the fundamental coupled interaction of charged Gossamer structures with the ambient charge flux can be experimentally investigated. Of interest are, will the EIMS remain inflated during the charge deflections, and are there visible charge flux interactions. Aluminum coated Mylar membrane prototype structures are created to test their inflation capability using electrostatic charging. To simulate the charge flux, a 5keV electron emitter is utilized. The remaining charge flux at the end of the test chamber is measured with a Faraday cup mounted on a movable boom. A range of experiments with this electron emitter and detector were performed within a 30x60cm vacuum chamber with vacuum environment capability of 10^{-7} Torr. Experiments are performed with the charge flux aimed at the electrostatically inflated membrane structure (EIMS) in both charged and uncharged configurations. The amount of charge shielding behind and around the EIMS was studied for different combinations of membrane structure voltages and electron energies. Both passive and active shielding were observed, with active shielding capable of deflecting nearly all incoming electrons. The pattern of charge distribution around the structure was studied as well as the stability of the structures in the charge flow. The charge deflection experiments illustrate that the EIMS remain inflated during charge deflection, but will experience small amplitude oscillations. Investigations were performed to determine a potential cause of the vibrations. It is postulated these vibrations are due to the charge flux causing local membrane charge distribution changes. As the membrane structure inflation pressure is changed, the shape responds, and causes the observed sustained vibration. Having identified this phenomenon is important when considering electrostatically inflated membrane structures (EIMS) in a space environment. Additionally, this project included a study of membrane material impacts, specifically the impact of membrane thickness. Extremely thin materials presented new challenges with vacuum preparation techniques and rapid charging. The thinner and lighter membrane materials were successfully inflated using electrostatic forces in a vacuum chamber. However, care must be taken when varying the potentials of such lighter structures as the currents can cause local heating and melting of the very thin membranes. Lastly, a preliminary analysis is performed to study rough order of magnitude power requirements for using EIMS for radiation shielding. The EIMS power requirement becomes increasingly more challenging as the spacecraft voltage is increased. As a result, the emphasis is on the deflection of charges away from the spacecraft rather than totally stopping them. This significantly alleviates the initial power requirements. With modest technological development(s) active shielding is emerging to be a viable option.

Table of Contents

1. Project Overview

Radiation protection and shielding for human space missions has been identified as a technical area by the NASA's Office of the Chief Technologist (OCT) and has been detailed in section 6.5 of TA06 and mentioned in other sections and technical areas. Exposures from the hazards of severe space radiation in deep space/long duration missions are very different from that of low earth orbit, and much needs to be learned about their effects. However, it is clear that revolutionary technologies will need to be developed. The current conventional radiation protection strategy based on materials shielding alone, referred to as passive radiation shielding, is maturing (has been worked on for about three decades) and any progress using the materials radiation shielding would only be evolutionary (incremental) at best. The overall situation is further augmented by the nonexistence of *in vivo* or *in vitro* data or studies about *continuous* long duration tissues exposure to radiation and concomitant biological uncertainties. Material shielding would have only limited or no potential for avoiding *continuous* exposure to radiation. Besides, current material shielding alone for radiation protection for *long duration/deep space safe human space missions has been shown to be prohibitive due to pay load and cost penalties and is not a viable option. Material shielding is low earth orbit (LEO) technology*. Revolutionary comprehensive technologies are needed, while taking full advantage of advances in the state-of-the-art evolutionary material shielding.

1.1 Brief Introduction

The breakthrough in radiation protection for a long duration space mission would have to come from active radiation shielding and biology. The biggest advantage of using active radiation shielding is the significant reduction of biological risks, often unknown, that are always present with the use of bulk material shielding in manned spacecraft due to primary space and secondary, material shield generated radiation. *During Phase I electrostatic active radiation shielding technology has significantly been advanced to a much higher maturity and/or TRL level than ever before and has moved a step closer to reality.* It is ready to be folded with other radiation protection technology options develop, design and deploy the viable comprehensive space radiation protection technology for future deep space human missions.

We explored active methods to perform radiation shielding using lightweight Gossamer structures. The goal is to develop comprehensive active radiation shielding and fold it with the state-of-the art material radiation shielding using lightweight structures to deflect away radiation from the safe-zone habitat area as shown in figure 1. The novel aspect is that 1) large-scale force field using distributed charge surfaces is considered (Tripathi et al., Advances in Space Research, 42 (1008) 1043-1049—by investigating and optimizing the mesh-type and gossamer like deployable structures), and 2) that the electrostatic charges was exploited to inflate or actuate extremely lightweight Gossamer membrane structures, as demonstrated during Phase I study and also in (Stiles et al., AAS/AIAA Astrodynamics Specialist Conference, Toronto, Canada AIAA-2010-8134), 3) further synergistically augmented the structure with current carrying ring/toroidal structure, generating safe level of magnetic field, thus further reducing radiation hitting the safe zone. This strategy seems to be the way forward for deep space human radiation protection.

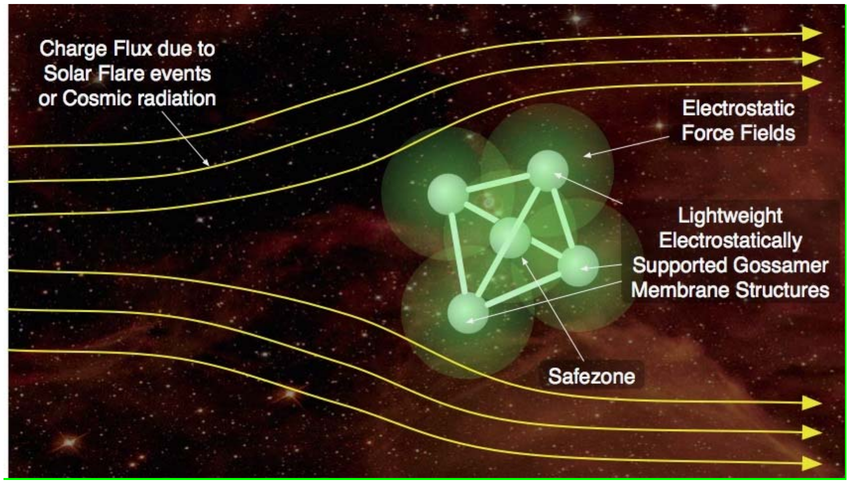

Figure 1. Illustration of Active Radiation Deflection using Electrostatic Gossamer Structures and current carrrying toroidal positioned about a Safezone.

Recently, a peer reviewed journal article from Langley (Tripathi et al., Advances in Space Research, 42 (2008) 1043–1049; paper available on request) made a critical analysis and demonstrated why previous approaches of using electrostatic (discussed briefly under "*Some issues with previous electrostatic shielding and their resolution*") and magnetic radiation shielding were not feasible. However, the proof-of-concept of electrostatic active shielding using novel approaches and configurations was clearly established. The goal is to repel enough positive charge ions so that they miss the spacecraft without attracting thermal electrons. During phase I several aspects of the technology were validated using lightweight Gossamer structures.

Results were very promising and showed that ions of lower energies were completely blocked or deflected. Higher energy ion fluxes were reduced by certain amount depending upon the charge and mass of the radiation ion and the potential used in the shielding configuration. The electrostatic shielding is most effective for solar particle events (SPE), as this radiation is totally blocked or diverted. It also provides dramatic protection against galactic cosmic rays (GCR) and was found to be over 70% more effective than the best *current* state-of-the-art (hydrogen rich) material shielding.

Here, we established technological advancement of the demonstrated electrostatic active radiation shielding *by using and optimizing the mesh-type and gossamer like structures*; and demonstrated: 1) to use electrostatic active radiation shielding as a simple cost-effective strategy to deflect/stop space radiation from hitting the spacecraft, thus alleviating biological uncertainties and the risks, 2) further synergistically augmented the structure with current carrying ring/toroidal structure, generating safe level of magnetic field, thus further reducing radiation hitting the safe zone, and 3) to further mitigate exposure effects by using, *in concert*, the state-of-the-art evolutionary passive (material) shielding technologies for the much reduced and weaken radiation that may escape and hit the spacecraft. Deployable gossamer structures in an "umbrella like" configuration would be the cornerstone of the development. It may be noted that synergistic electrostatic active radiation and the low level of current carrying ring/toroidal option does not bring in additional biological harmful exposures, as in the case of active magnetic radiation shielding.

The dual strategy holds the promise of greatly reducing the penetration of high-energy GCR fluxes, with requiring magnetic fields to remain below critical bio-thresholds. Our preliminary investigations are very promising. The latter would be very beneficial from a bio-effects standpoint, since it would mitigate possible adverse effects of magnetic fields on biological tissues.

Inflatable charged gossamer structures (which mimic "anti-radiation umbrellas") could also be deployed on space vehicles and transportation platforms; with the advantage of mass-reduction and compactness. They would also have advantages of low field emission, "hits" from incident charged particles for lower power requirements, and better stability charge. *The electrostatic system can also be probed for dual use – not only in providing active shielding, but also in its potential use for electrostatic-based propulsion system for interplanetary missions.*

Some issues with previous electrostatic shielding and their resolution

Some of the problems with having *a pair of oppositely charged concentric spheres* [F.H. Volger, AIAA J., vol.2, pp. 872-878, 1964; S.W. Kash, Astronautics, vol. 7, pp. 68-75, 1962; W. Frisina, Acta Astronautica, vol. 12, pp 995-1003, 1985; and L.W. Townsend, Workshop Arona (Italy), May 27-31, 2007] are the dynamic stability issue, breakdown, mass penalty, and discharge. For example, a slight off-center displacement would result in the formation of an asymmetric force, leading the spheres to be quickly attracted towards each other.

Besides, the main issue with older concentric spheres' approaches was their configuration, as the goal was to totally stop the radiation; as a result, there was a need for huge power requirements. The selective deflection of positively and/or negatively charged radiation as it approached safe-zone was not possible in this configuration. The entire space radiation headed to the safe-zone. This was another reason of huge power requirement and contributed to their failure, in addition to the factors mentioned above. On the other hand, new approach separates the positively and negatively charged configurations and selectively deflects positively and negatively charged radiation prior to their approaching safe-zone. The emphasis in newer approach is on the early deflection of radiation rather than totally stopping them when they approach the safe-zone. This is a huge contributing factor that led to the success of the newer approach where previous approaches failed.

An area of concern for electrostatic shielding is the power consumption for keeping the shielding geometries continually charged. However, secondary emission depends on the contact surface area. As opposed to the older approach, the newer mesh-like material is a superior option than an all-solid structure. In fact, the larger the overall shielding system, the smaller is the fraction of the grid material. Making the grid members thinner and increasing the inter-grid spacing would be advantageous. This would leave fewer target areas/sites for high energy particles to collide, and hence, minimize the secondary emission and charge losses. A further advantage of the tenuous grid/mesh concept is the savings in mass and material costs.

The Langley approach [Tripathi et al., Advances in Space Research, 42 (1008) 1043-1049] is a novel innovative approach and was shown in the peer review article to be feasible. This approach does not require fully enclosing the spacecraft by solid electrostatic shielding material. For example, instead of repelling charged particles with high voltage as in previous approaches, the particles could be deflected just enough by applying relatively low voltages by the chosen configuration and would leverage with inflatable gossamer structures having meshed structure.

1.2 Some Phase I Highlights

- Experimentally demonstrated that lightweight Gossamer structures could enable active radiation shielding applications
- Experimentally validated electron deflection efficiency with charged Gossamer structures
- Experimentally and analytically studied several Gossamer shapes and materials to enhance deflection and stiffness
- Identified ~ 5 Hz structural vibrations due to electrostatic inflation and charge flux coupling
- Studied power requirements for deep space shielding
- Investigated a number of configurations including toroidal configuration
- Investigated ions and electrons trajectories for GCR, SPE, and nominal plasmas
- Investigated transmission probabilities for GCR ions (protons through iron) and SPE
- Published 1 journal paper; 5 conference papers; 4 reports

2. Configuration Studies

Developing successful and optimal solutions to mitigating the hazards of severe space radiation in deep space long duration missions is critical for the success of deep-space explorations, including the Moon, Mars and beyond. Space crews traveling aboard interplanetary spacecraft will be exposed to a constant flux of galactic cosmic rays (GCR), as well as intense fluxes of charged particles during solar particle events (SPEs). A recent report (Tripathi et al., 2008) had explored the feasibility of using electrostatic shielding in concert with the state-of-the-art materials shielding technologies. Here we continue to extend the electrostatic shielding strategy and quantitatively examine a different configuration based on multiple toroidal rings. Our results show that SPE radiation can almost be eliminated by these electrostatic configurations. Also, penetration probabilities for novel structures such as toroidal rings are shown to be substantially reduced as compared to the simpler all-sphere geometries. More interestingly, the dimensions and aspect ratio of the toroidal rings could be altered and optimized to achieve an even higher degree of radiation protection.

2.1 Introduction

One of the biggest obstacles to human space exploration of the solar system is the health risk posed by prolonged exposure to space radiation. Space crews traveling aboard interplanetary spacecraft will be exposed to a constant flux of galactic cosmic rays (GCR), as well as intense fluxes of charged particles during solar particle events (SPEs). Unlike astronauts serving aboard the International Space Station (ISS), space crews aboard interplanetary spacecraft (such as the mission of Mars envisioned by NASA) would not be protected by the Earth's magnetosphere. An additional difficulty is that crews would be exposed to the harsh radiation environment for extended periods of time. Estimated transit times for a human mission to Mars vary from 100 to 150 days each way with a possible extended duration stay on Mars estimated to be 200 days (Hoffman and Kaplan, 1997).

Naturally as a result, a strong focus on the safety of the missions and the crew for long duration space missions has begun to emerge as a critical component of planning and design. Based on conventional radiation shielding strategies, an interplanetary spacecraft will require substantial shielding 50 g/cm^2 of aluminum by one estimate (Wilson et al., 2001) if the 50 mSv limit for astronaut exposure is to not be exceeded. Though other materials (including carbon nanotube-based shielding) might reduce the weight somewhat, these passive shielding strategies amount to adding ‘‘dead mass’’ to a spacecraft which is not an economically viable solution. Besides, passive shielding can lead to the production of energetic high-energy secondary radiation. Hence, considerations of active shielding (Townsend, 1983; Sussingham et al., 1999; Smith et al., 2006), especially against the high-energy heavy ions present in galactic cosmic rays, become germane and important. Though magnetic shielding appears to be a possibility (Cocks, 1991) there are some serious drawbacks to this technology. These issues include: (a) Requirements of large currents to produce magnetic fields of ~20 Tesla (Spillantini et al., 2007). (b) Large power demands on a cryo-cooling system for supporting high-T_c superconductors for the magnetic fields, and (c) the adverse effect of magnetic fields on biological tissues itself (Kinouchi et al., 1996; Kawakubo et al., 1999; Nittby et al., 2008). For this reason, here we choose to turn to the alternate electrostatic shielding. Electrostatic shielding based on charged spheres has been discussed (e.g., Smith et al., 2006). Numerical techniques for evaluating the effectiveness of such spherical geometries, in this context, have also been reported (e.g., Metzger and Lane, 2009). A rigorous analysis was recently presented for a new configuration of electrostatic active shielding (Tripathi et al., 2008). Relevant comparisons were also made with the state-of-the-art passive shielding material. It was argued that electrostatic shielding would have an advantage due to ‘blocked’ space radiation spectrum, particularly in view of the unknown biological uncertainties for long duration space radiation exposure. Though promising, achieving even more optimized results in terms of alternate configurations need to be investigated.

While the particle flux for SPE falls off steeply with increasing energy and is typically below 100 MeV per nucleon, the GCR spectrum peaks at values slightly lower than 1 GeV per nucleon before falling off (Yao et al., 2006). Furthermore, it is generally agreed that particles with energies of 1–4 GeV per nucleon are the most damaging to humans (Schimmerling and Cucinotta, 2006). Hence from the standpoint of practical utility, it is important to safeguard against the more energetic GCR influx. The previous electrostatic configuration based on two sets of negatively (outer) and positively (inner) spheres still led to transmission levels over 80% in this energy range. In an effort to improve the outcome, here we continue to probe the electrostatics based active-shielding strategy for a toroidal ring geometry. Specifically, as shown in Fig. 1a, the configuration consists of three different inner rings kept at a positive voltage and six outer spheres. For comparison, the twelve-sphere geometry as previously reported (Tripathi et al., 2008) is also included in this contribution. The six outer negatively charged spheres are designed to play a role in repelling the free electrons from the solar wind (Townsend, 1984). Without such protection against the negative charge, three potential problems could arise: (a) electrons accelerated due to the positive potential would become dangerous to the astronauts and pose substantial health risks, (b) the acceleration would lead to excessive Bremsstrahlung levels, and (c) the electron current collected by the shielding elements (e.g., the toroidal rings) held at positive potential would annihilate the charge and lead to enhanced power requirements to maintain an effective electrostatic shield.

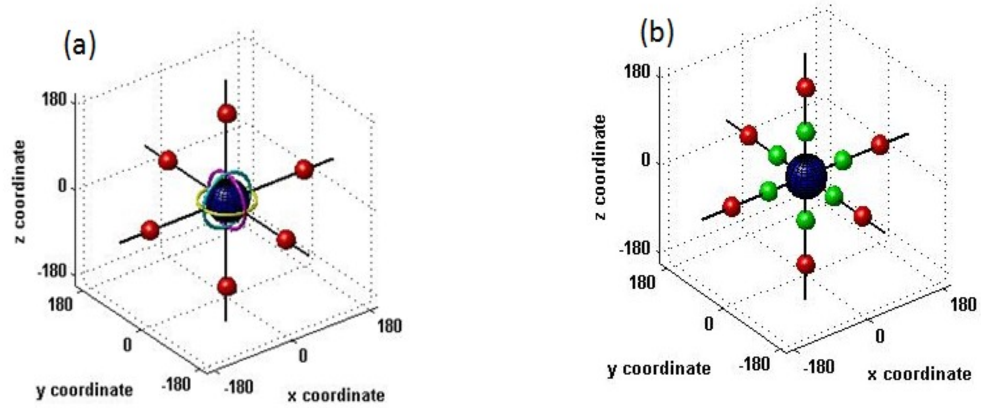

Fig. 1. Geometries considered for electrostatic shielding. (a) Three toroidal rings with six negatively charged spheres, and (b) a twelve-sphere configuration previously reported.

In this brief report, we investigate an alternative three-ring configuration as shown in Fig. 1a. This structure will be shown to lead to superior blocking characteristics over the previous all-sphere geometry. A simple extension can then be the replacement of the outer negative spheres with three larger toroidal rings held at a negative potential. We also show and discuss the effect of ring radius on the overall effectiveness.

2.2 Simulation method

For a given potential configuration, the influence that the electrostatic fields have on incident charged particles via the collective Coulomb forces can lead to regions of space within which particles below some energy are unable to enter. These "forbidden" regions of space are said to be shielded from the incoming particles. In the simplest configuration of Fig. 1b, there are six charged spheres, each at potential V_j and having an associated charge Q_j on the surface. The equation of motion of a particle with charge q_i, moving with velocity $\boldsymbol{v}_i$ in a collective electrostatic field is given by:

$$\gamma m_i \, d\mathbf{v}_i/dt = \sum_j q_i \mathbf{E}_{ij} = \sum_j q_i Q_j (\mathbf{r_i} - \mathbf{r_j})/[4\pi\varepsilon_0 \, |\mathbf{r_i} - \mathbf{r_j}|^3] \quad , \qquad (1)$$

where m_i is the rest mass of the i^{th} particle, $\boldsymbol{r}_i$ and $\boldsymbol{r}_j$ are the position vectors of the incoming particle and the center of the sphere held at a surface potential V_j, respectively. Also, in the above equation, the summation is over all the charged spheres in the shielding configuration, $\gamma = (1 - |\mathbf{v}_i|^2/c^2)^{½}$ is the relativistic correction factor, c is the speed of light, ε_0 is the free-space permittivity, and $\mathbf{E}_{ij}$ the electrostatic field at the location of the charge q_i.

The potential and electric field distributions for toroidal rings are somewhat different from those created by charged spheres. The electrostatic shielding in this contribution is taken to consist of three doughnut-shaped toroidal rings with axial symmetries along the x-, y- and z-directions. For simplicity, figure 2 shows only one ring being considered around the z-axis.

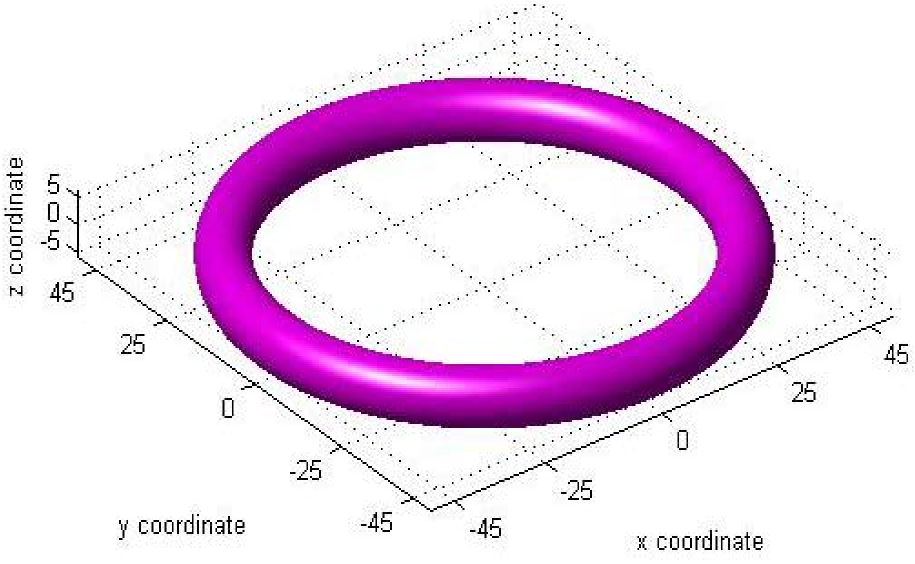

Fig. 2. Toroidal ring geometry for simple analysis.

The mean radius of the torus in the z=0 plane is 45 meters with a thickness of 10 meters. Given the geometry, the toroidal co-ordinate system is best suited for the analyses.

Using the notation (v,u,Φ), the toroidal coordinates are related to the usual Cartesian coordinates (x,y,z) as:

$$x = A \sinh(v) \cos(\Phi)/[\cosh(v) - \cos(u)] \quad , \tag{2a}$$

$$y = A \sinh(v) \sin(\Phi)/[\cosh(v) - \cos(u)] \quad , \tag{2b}$$

$$z = A \sin(u) /[\cosh(v) - \cos(u)] \quad . \tag{2c}$$

The coordinates are restricted to the domain: $v \in [0,\infty]$, $u \in [0,2\pi]$, and $\Phi \in [0,2\pi]$. Here, if "a" denotes the mean radial distance to the toroid from the center, and "b" the thickness of the torus in the z=0 plane, then the toroidal surface is given by values of constant $v = v_0 = \mathrm{Ln}[(a/b)+\{(a/b)^2-1\}^{½}]$, and also satisfies the equation: $z^2 + [(x^2 + y^2)^{½} - A \coth(v_0)]^2 = [A/\sinh(v_0)]^2$. In this notation, the parameter A of eqn. (2) is related to the mean radial distance "a" as: $A = a \tanh(v_0)$, and also to the parameter "b" as: $A = b \sinh(v_0)$. Thus, in this system, distances from the center (in the z=0 plane) to the inner and outer rims of the torus are "a-b" and "a+b", respectively. The inverse transformations are given by:

$$\Phi = \tan^{-1}(y/x) \quad , \tag{3a}$$

$$v = \mathrm{Ln}(d_1/d_2) \quad , \tag{3b}$$

$$u = \cos^{-1}[\{d_1^2 + d_2^2 - 4A^2\}/(2\, d_1 d_2)] \quad , \tag{3c}$$

$$\text{where } d_{1,2} = [(x^2 + y^2)^{½} \pm A)^2 + z^2]^{½} \quad . \tag{3d}$$

In the present scenario, the toroidal ring was taken to be charged and held at a constant potential V_0. The potential around the ring can then be conveniently obtained by solving the Laplace equation, with the assumption that the deep-space environment has no atmosphere and negligible charge density. The governing equation can be written (Morse and Feshbach, 1953) as:

$$\{\delta[\sinh(v)\, \delta F/\delta v]/\delta v\}/\sinh(v) + \delta^2 F/\delta v^2 + \{\delta^2 F/\delta \Phi^2\}/\sinh^2(v) + F/4 = 0 \quad , \tag{4}$$

where the required voltage $V(v,u,\Phi)$ is expressed in terms of $F(v,u,\Phi)$ as: $V = [\cosh(v)-\cos(u)]^{½} F(v,u,\Phi)$. The solution to this Dirichlet problem then works out to:

$$V(v,u,\Phi)=(V_0/\pi)[2\{\cosh(v)-\cos(u)\}]^{½}{}_{n=0}\sum^{\infty}[Q_{n-½}(\cosh(v_0))/P_{n-½}(\cosh(v_0))]P_{n-½}(\cosh(v))\cos(nu). \tag{5a}$$

In the above, $P_{n-½}(x)$ and $Q_{n-½}(x)$ are the Legendre functions of the first and second kind, respectively, of degree n-½ .

Based on the solution from eqn. (5a), results for the potential due to a toroidal ring with mean radius a = 45 meters, thickness b = 5 meters, with its surface held at 300 MV are shown in Fig. 3. The surface voltage of 300 MV was taken to match the value of a previous report (Tripathi et al., 2008). As expected the values are the highest in the equatorial plane and fall off along with distance along either direction of the z-axis.

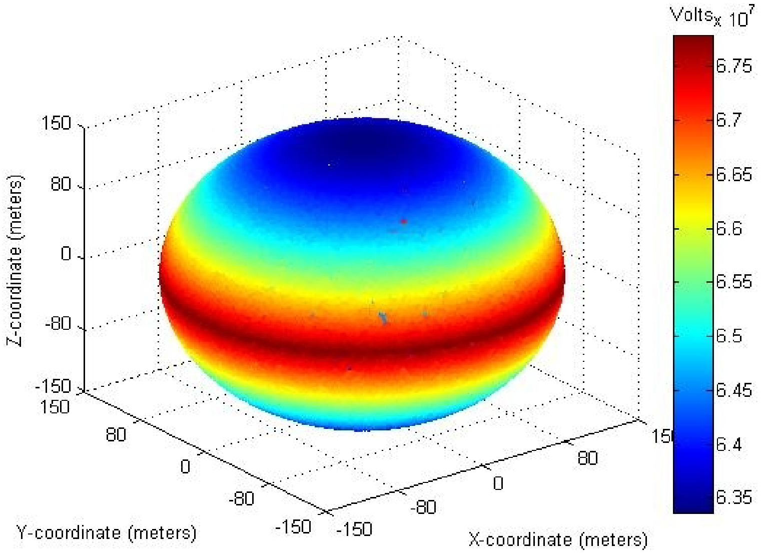

Fig. 3. Potential profile of a toroidal ring held at a 300 MV potential.

Based on Eqn. (5a), the charge Q on each ring required to maintain the toroidal structure at a particular value of constant potential V_0 can be obtained through Gauss' law. Thus:

$$Q = \varepsilon_0 \iint E\, h_v\, h_\Phi \; d\Phi \; du \quad , \qquad (5b)$$

where , h_u and h_Φ are the scale factors (or metric coefficients from which the Lame´ factors can be obtained) associated with the differentials "du" and "dΦ". For the toroidal system chosen:

$$h_u = h_v = A/[\cosh(v) - \cos(u)] \quad , \qquad (5c)$$

$$\text{and,} \quad h_\Phi = A \sinh(v)/[\cosh(v) - \cos(u)] \quad . \qquad (5d)$$

Here since dV/dv is independent of Φ, and hence one gets:

$$Q = -2\pi\varepsilon_0 A \; {}_0\!\int^{2\pi} \{(dV/dv)\, \{\sinh(v_0)/[\cosh(v_0)\text{–}\cos(u)]\}\, du \;\equiv\; Q(V_0) \; . \qquad (5e)$$

Since the potential around the ring is determined by the bias V_0 [as given in eqn. (5a)], the dV/dv term in eqn. (5e) implicitly involves this applied voltage [i.e., $Q \equiv Q(V_0)$]. Consequently, the total charge becomes a function of V_0. The electric field E normal to the constant $v = v_0$ surface, required in Eqn. (5b) can be obtained in a straight-forward manner as:

$$E = -(dV/dv)/h_v = -(dV/dv)\,[\cosh(v) - \cos(u)]/A \; . \qquad (5e)$$

Thus by computing the total charge $Q(V_0)$ on the ring at a given voltage, the energy expended to build up the requisite potential [= $Q(V_0)\, V_0/2$] can easily be computed.

In our calculations, three toroidal rings are used with their axes of symmetry along the x-, y- and z-directions. The potential along the <111> direction for such a three-ring configuration (with all three surfaces held at 300 MV) is shown in Fig. 4. For comparison, the potential profile along this same <111> direction for a six-sphere configuration positioned on either sides of the three axes and held at 300 MV is also shown. To maintain some degree of geometric equivalence between the two configurations, each sphere was taken to have a radius of 10 meters with their centers on the three axes located 50 meters from the center. The profile of Fig. 4 brings out the advantage of the toroidal configuration. The potential is seen to be much higher with a sharper gradient (especially for the shorter distances) which create larger electric fields.

Here calculations for charged particle penetration have been performed using Monte Carlo simulations for the specified electrostatic configurations, i.e., toroidal and spherical geometries in the present case. The kinetic-based, Monte Carlo numerical simulations followed the trajectories of 10,000 particles. These particles were taken to be injected inwards at random angles from a spherical simulation boundary of radius 150 meters. Trajectories of each ionized particle were computed based on the relativistic equations of motion. The electrostatic driving force (= $-q \sum \blacktriangledown V_i$) from the three toroidal rings was dynamic, based on the instantaneous position of the particle from the charged surfaces. By tracking the trajectories of all the 10,000 simulated particles, this process naturally allowed for the evaluation of the fraction penetrating the central region, those completely deflected by the electrostatic shielding arrangement, and the fraction incident onto the charged rings. The latter helps provide a measure of the rate of charge annihilation (and hence, voltage discharge) for a given space-environment and flux density for the spherical and toroidal geometries.

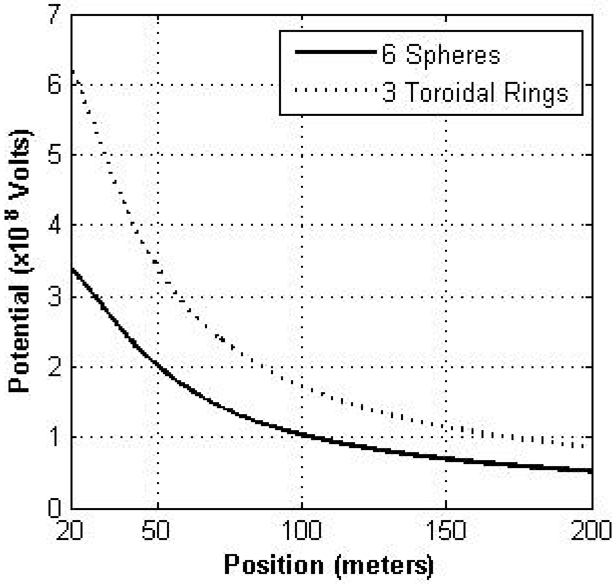

Fig. 4. Potential profile along the <111> direction for a three toroidal rings with each geometric surface maintained at a 300 MV bias. Potential for 6 spheres is also shown for comparison.

In order to accurately gauge space radiation responses to the shielding system via the Monte Carlo simulations, one has to first mimic the characteristics of both solar particle events (SPEs) and galactic cosmic rays (GCRs), and their respective energy-dependent fluxes. The solar activity cycle is approximately 11 years long (Rossi, 1964) with about seven years of solar maximum. The published compilation of fluence spectra for the larger solar particle events (Wilson et al, 1999) can serve as a convenient data set. It is believed that there are two categories of solar particle events and that each one accelerates particles in a distinct manner (Reames, 1999). Solar flares have characteristics that tend to be electron rich, last for hours, and have unusually high ^{3}He content relative to ^{4}He and have low energy. On the other hand, Coronal Mass Ejection (CME) is a large eruption of plasma that drives a shockwave outward, tends to be proton rich, last for days, and has small ^{3}He content relative to ^{4}He and are of higher energy range of up to a hundreds of MeV range and are often use for radiation shield design. Here, for purposes of a more realistic and critical simulation assessments of the shielding capability for the electrostatic configurations, the longer-term CME events were used. A description of the integral SPE flux φ used here, can be expressed as (Webber, 1963):

$$\Phi = 10^9 \exp[\{239.1 - (E\{E+1876\})^{½}\}/100] \text{ cm}^{-2} . \tag{6}$$

For GCR, the model spectra (Badhwar and O'Neill, 1994) was used here since it is commonly used for space missions design investigations. A sample plot of the energy-dependent differential flux for galactic cosmic ray radiation is shown in Fig. 5 for a few representative ions. The peak is seen to occur at energies slightly below 1 GeV per nucleon.

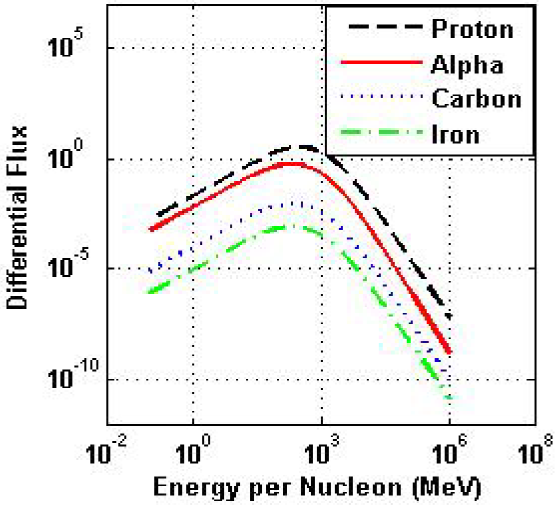

Fig. 5. Plot of the differential flux for a few select ions comprising the GCR spectra.

2.3 Results and Discussion

Numerical simulations were carried out to obtain particle trajectories based on equation (1). Each incident ion was taken to have the same initial starting energy, but assigned random position on a starting spherical surface. The initial velocities were also chosen to have random components, but in an inward direction. The Crank-Nicholson scheme was used which is an implicit, second-order method in time, and is numerically stable. A very small time step of 2 ps was chosen.

Simulation results obtained for SPE and GCR protons for the 12-sphere configuration are shown in Fig. 6. For concreteness the differential flux and the probability of protons hitting any one of the six outer negatively charged spheres are both shown. The six outer negatively charged spheres (as shown in Fig. 1b) were taken to be at a -100 MV potential, while the six inner positively charged spheres were each set at 100 MV. The radii of the outer and inner spheres were 20 and 10 meters, respectively, and their locations were at mean distances of 160 and 50 meters, respectively from the center. As might be expected, at lower energies there is a stronger possibility for the protons to be captured by the set of six negatively charged outer spheres. These results can be used to evaluate the voltage discharge rate of the negative spheres and allows the average power loss from SPE collisions of various ions to be obtained.

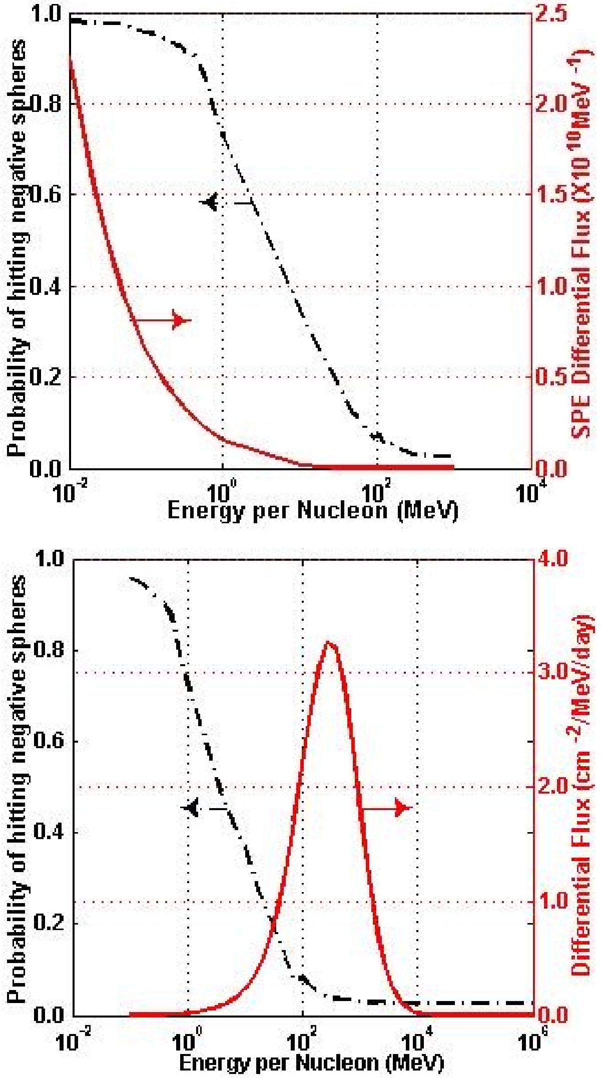

Fig. 6. Differential flux and computed probability of proton capture by the set of twelve charged spheres due to: (a) SPE radiation, and (b) protons from incident GCR flux.

Extending the calculations to alphas particles and iron ions in the GCR spectra yielded the results shown in Fig. 7. For GCR, the probability and flux curves have much less overlap (as compared to SPE), which is indicative of a negligible contribution to voltage discharging.

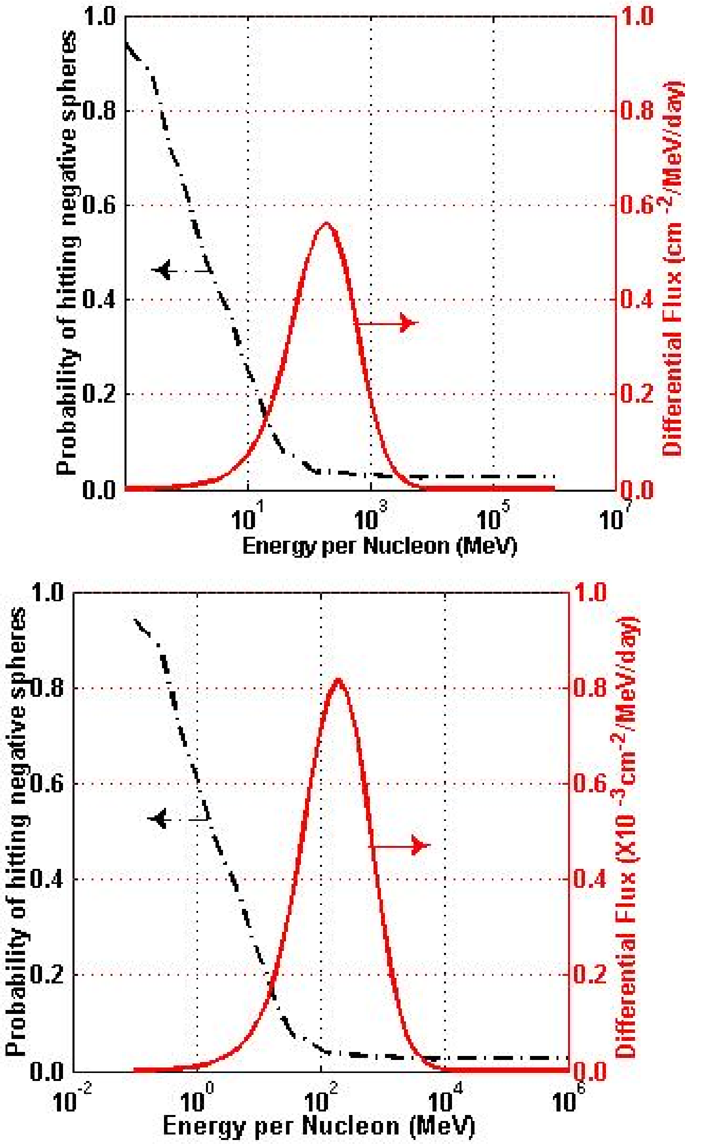

Fig. 7. Differential flux and computed probability of alpha and iron ion capture by the negatively charged spheres due to incident GCR flux. (a) Incident alpha particles, and (b) iron ions. The differential flux is also shown for clarity.

The reduced overlap decreases the probability of a collision with the outer negative spheres, and makes voltage discharging (and hence the need to replenish and re-power the negative spheres) even more negligible. Overall, our calculations for SPE protons yielded a reduction of only ~1.163 Volts per Solar Particle Event based on the numerical values of the “hitting probability”. This is clearly negligible compared to the assumed 100 MV initial bias. The computed values of power loss from GCR particle collisions were: 0.16462 mW (due to protons), 0.07234 mW (for alpha particles), and 1.587 μW (for Iron ions).

Next, predictions of the three-toroidal ring configuration (Fig. 1a) were compared to the results of the all-sphere geometry (Fig. 1b). For a realistic head-to-head comparison, the energy requirement for the two configurations was intentionally maintained at the same fixed level. This meant adjusting the equipotential across each of the three rings, and was carried out as follow. First, for the all-sphere configuration, the charge Q associated with a positive sphere of radius "a" (= 10 meters) held at a potential V_0 of +100 MV was computed as: $Q = 4\pi a\varepsilon_0 V_0 = 0.11121$ Coulombs. For the 6 inner positive spheres, this then leads to an overall energy of $3.3363\text{x}10^7$ Joules [= $6(0.5\ Q\ V_0)$]. An equivalent energy for the ring toroidal configuration, then places a condition on the potential V_0 such that: $0.5\text{x}V_0\ Q(V_0)\text{x}3 = 3.3363\text{x}10^7$ as well in order to match the energy for the all-sphere configuration. Using eqns. 5(e)-5(f) these quantities can be evaluated. The results upon numerical evaluation for the three toroids at "a" = 45 meters and "b"= 10 meters, yield a potential of about 50 MV for equivalent energy.

To gauge the performance based on this common energy requirement, simulations were carried out to compare proton transmission probabilities for the configuration involving the 6 negative and 6 positive spheres held at $\pm$ 100 MV, and the alternate geometry consisting of 3 rings at 50 MV and 6 outer negative spheres held at -100 MV. As mentioned above, the radii of the inner positive spheres were 10 meters, while the "a" and "b" parameters for the three toroids were taken to be 45 meters and 10 meters, respectively. As evident from Fig. 8, a significant lowering in the transmission probability is predicted for the configuration involving the three inner toroids. This reduction occurs at the high particle energies beyond the 200 MeV range, a regime that typically applies to GCR radiation. This reduction is occurs in spite of the toroidal voltage having been reduced down to +50 MV from the +100 MV value for the six-positive sphere case. Furthermore, though not explicitly shown here, further benefits can be expected by also replacing the six outer negative spheres by three corresponding negatively charged toroidal rings having a suitably larger radius "a".

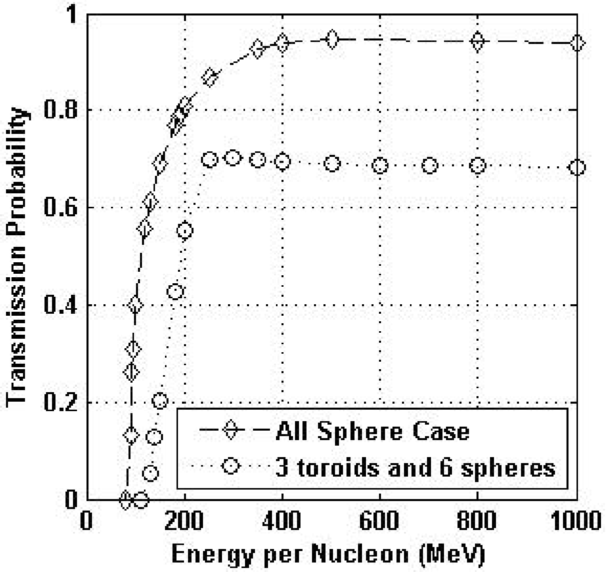

Fig. 8. Predicted transmission probabilities of GCR protons to penetration through an inner 20 meter spherical zone. Simulations were aimed at comparing the all sphere geometry of Fig. 1b and the toroidal configuration of Fig. 1a based on an equal-energy criteria.

Finally, for completeness, the role of structural dimensions for the toroidal rings were examined. One expects a torus with a larger radius to be better able to block incoming ions given its larger volume. In order to probe this quantitatively, simulations were performed for incoming protons for the three-ring configuration at the same 50 MV biasing, but for different values of the b-parameter for the toroidal ring. The results are shown in Fig. 9. With increasing value of the radial parameter b, the transmission probability is predicted to progressively decrease. In fact for a=45, the limiting probabilities drop from ~0.95 for b=1 meter down to ~0.45 at b=10 meters. This not only underscores the inherent advantage of the toroidal structure, but points towards construction of larger radii tori for more effective electrostatic active shielding. The only conceivable downside might be in terms of the larger size and volume of the shielding structure. However, if advances in the flexible gossamer materials (or even mesh-like structures) are employed to advantage, this possible inconvenience associated with a larger structural mass can be overcome. It may be mentioned that the transmission probability in the 700-1000 MeV range over which the GCR spectra peaks (as in Fig. 5), is substantially reduced.

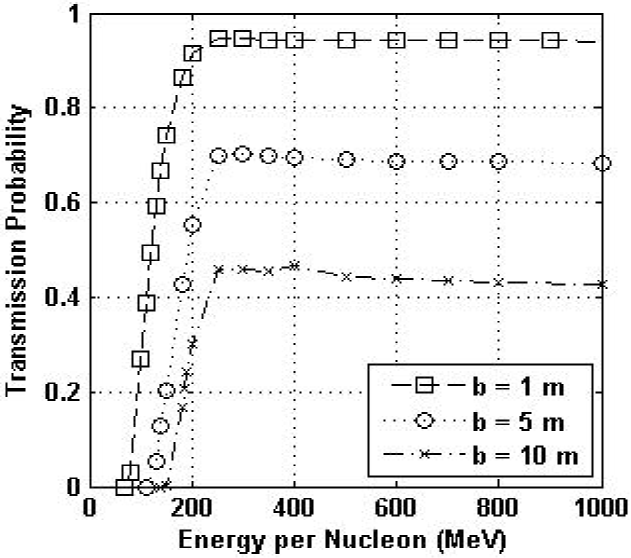

Fig. 9. Predicted proton transmission probabilities for the three-ring toroidal configuration for a = 45 meters, but for three different values of the b-parameter.

2.4 Summarizing conclusions

We have made detailed studies to evaluate a toroidal configuration for its potential towards electrostatic shielding. An all-sphere structure previously proposed was included to provide a reference and convenient comparison. The SPE radiation was shown to be almost eliminated by these electrostatic configurations. Furthermore, it was shown that the power needed to replenish the electrostatic charges on the all-sphere shielding configuration due to particle hits from the GCR and SPE radiation is minimal and insignificant. Most importantly, it was shown that novel structures such as toroidal rings appear to be very promising. The penetration probabilities were shown to be substantially reduced as compared to the simpler geometries involving spheres, especially at the higher energies that characterize GCR spectra. Comparisons were also made between the two configurations at a fixed common energy. The results showed substantial improvements in shielding, even at the high energies above 200 MeV per nucleon. Our simulations also showed that the dimensions and aspect ratio of the toroidal rings could be altered to achieve an even higher degree of radiation protection. Finally, a simple extension can then be the replacement of the six outer negative spheres with three larger toroidal rings held at a negative potential.

2.5 References

Badhwar, J.D., O'Neill, P. M., An improved model of GCR for space exploration mission, Nucl. Tracks, Radiation Measurements, 20, 403 - 410, 1992.

Cocks, F.H. A Deployable High Temperature Superconducting Coil (DHTSC): A novel concept for producing magnetic shields against both solar flare and galactic radiation during manned interplanetary missions. J. British Interplanetary Soc., 44, pp. 99–102, 1991.

Hoffman, S.J., Kaplan, D.I. Human Exploration of Mars: The Reference Mission of the NASA Mars Exploration Study Team. NASA Johnson Space Center, Houston, TX, NASA Special Publication 6107, 1997.

Kawakubo, T., Yamauchi, K., Kobayashi, T. Effects of magnetic field on metabolic action in the peripheral tissue. Journal of Applied Physics, Part 2: Letters, 38, pp. L1201-L1203, 1999.

Kinouchi, Y., Yamaguchi, H., Tenforde, T.S. Theoretical analysis of magnetic field interactions with aortic blood flow. Bioelectromagnetics, 17, pp. 21-32, 1996.

Metzger, P. T., Lane, J.E. Electric potential due to a system of conducting spheres. The Open Applied Physics Journal, 2, pp. 32-48, 2009.

Morse, P.M., Feshbach, H. Methods of Theoretical Physics. McGraw-Hill Company, New York, New York, 1953.

Nittby, H., Grafström, G., Eberhardt, J.L., Malmgren, L., Brun, A., Persson, B.R.R., Salford, L.G. Radiofrequency and extremely low-frequency electromagnetic field effects on the blood-brain barrier. Electromagnetic Biology and Medicine, pp. 103-126, 2008.

Rossi, B. Cosmic Rays. McGraw-Hill, New York, 1964.

Reames, D.V. Particle acceleration at the sun and in the heliosphere. Space Sci. Rev., 90, pp. 413–491, 1999.

Schimmerling, W., Cucinotta, F.A. Dose and dose rate effectiveness of space radiation. Radiation Protection Dosimetry 122, pp. 349–353, 2006.

Smith JG, Smith T, Williams M, Youngquist R, Mendell W. Potential polymeric sphere construction materials for a spacecraft electrostatic shield. NASA/TM—2006-214302. Hampton, VA, Langley Research Center 2006.

Spillantini, P., Casolino, M., Durante, M., Mueller-Mellin, R., Reitz, G., Rossi, L., Shurshakov, V., Sorbi, M. Shielding from cosmic radiation for interplanetary missions: Active and passive methods. Radiation Measurements, 42, pp. 14 - 23, 2007.

Sussingham, J.C., Watkins, S.A., Cocks, F.H. Forty years of development of active systems for radiation protection of spacecraft. J. Astronaut. Sci. 47, 165–175, 1999.

Townsend, L.W. HZE particle shielding using confined magnetic fields, J. Spacecraft Rocket 20, 629–630, 1983

Townsend, L. W. Galactic heavy-ion shielding using electrostatic fields. NASA Technical Memorandum 86255, 1984.

Tripathi, R.K., Wilson, J.W., Cucinotta, F. A., Nealy, J. E., Clowdsley, M.S., Kim, M.Y., "Deep space mission radiation shielding optimization," 2001 International Conference on Environmental Systems, July 9-12, 2001, Orlando, FL; SAE 01ICES 2326, 2001.

Tripathi, R.K., Wilson, J.W., Youngquist, R.C. Electrostatic space radiation shielding. Advances in Space Research, 42, pp. 1043-1049, 2008.

Webber, W.R. An evaluation of the radiation hazard due to solar particle events. Boeing Report D2-90469, Aerospace Division, The Boeing Company, 1963.

Wilson, J.W., Cucinotta, F.A., Kim, M.H., Schimmerling, W. Optimized shielding for space radiation protection. Phys. Med. XVII (Suppl. 1), 2001.

Wilson, J.W., Cucinotta, F.A., Shinn, J.L., Simonsen, L.C., Dubey, R.R., Jordan, W.R., Jones, T.D., Chang, C. K., and Kim, M.Y. Shielding from solar particle event exposures in deep space. Radiation Measurements, 30, pp. 361-382, 1999.

Yao, W.M. et al., Review of Particle Physics. J. Phys. G: Nucl. Part. Phys. 33, pp. 245–251, 2006.

3. Charge Deflection Studies

3.1 Motivation

Radiation shielding is an important design criterion for any space mission, especially those involving human space explorers. A long-term goal for NASA is to use lightweight structures for active radiation shielding to create safe habitation zones. An example of this is charged membrane structures deflecting the harmful radiation ion-flux as seen in Figure 1 (Section 1.1). This report describes an investigation into the use of electrostatic fields for radiation shielding through such charged membrane structures. The membrane structures consist of layers of conducting material which self-repel to inflate when an absolute charge is applied. The electrostatically inflated membrane structure (EIMS) is envisioned as a lightweight structure that can act as shield to charged particles.

An experimental setup was designed to study the use of EIMS for charge deflection. An electron source and detector were mounted on opposite sides of an EIMS in a vacuum chamber. Experiments were performed to study the radiation shielding capabilities, the charge deflection pattern, and the stability of the structure. The report will discuss the hardware and software development for experiments, the membrane structure shapes, as well as a discussion on power requirements.

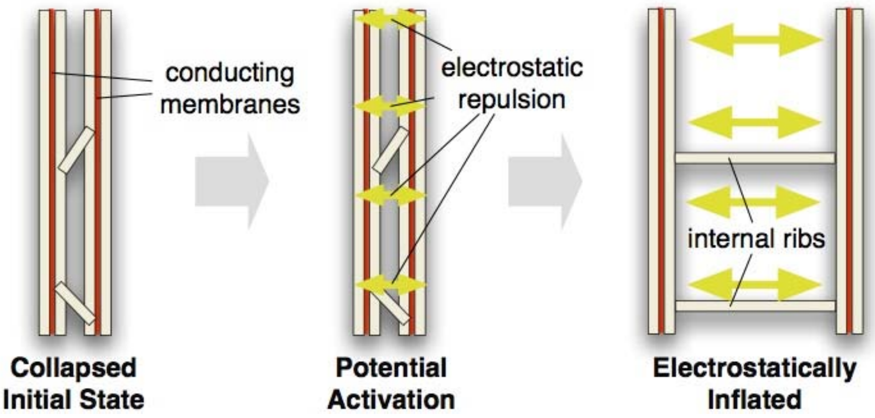

Figure 3.1: Illustration of electrostatic inflation of a membrane structure. The membrane interconnects (ribs) limit the amount of expansion and control the EIMS shape and thickness

3.2 EIMS Background

Electrostatically Inflated Membrane Structures or EIMS employ layers of lightweight membrane with a conductive coating along with active charge control to create inflationary electrostatic forces as shown in Figure 3.1. With this concept, extremely large deployed to stored volume ratios are feasible. The stored membrane structure will be packaged very tightly and does not require any pressurized gas storage devices. Rather, active charge control in the form of charge emission is employed to control the absolute EIMS potential. With EIMS it is feasible that the deployed structures are open shapes. Punctures due to micro-meteorites will have a negligible impact as this concept does not suffer from leakage concerns like gas-inflated Gossamer structures.

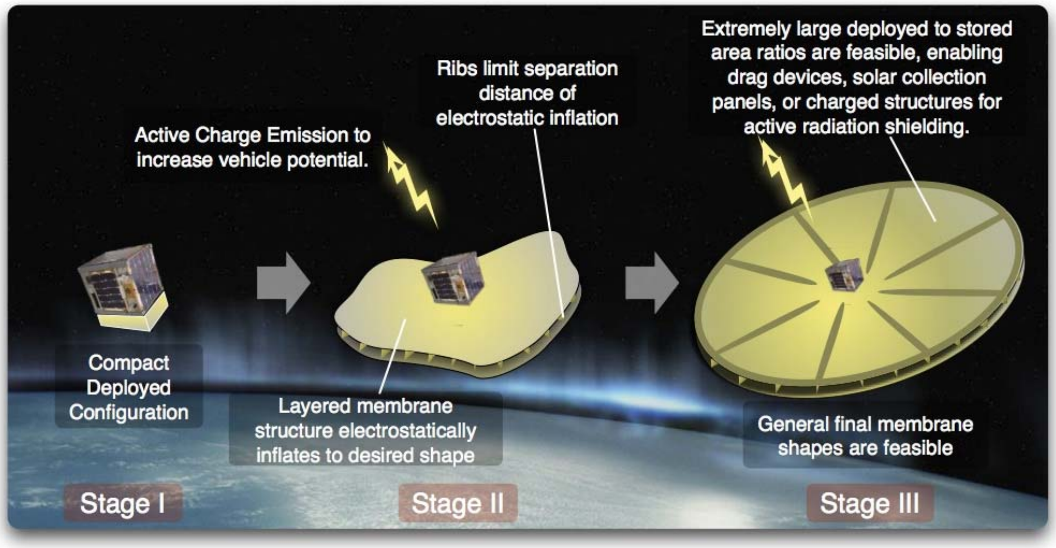

Figure 3.2: Electrostatic inflation concept illustration

An illustration of the EIMS concept deploying on a small satellite is shown in Figure 3.2. This concept of electrostatic inflation of membrane space structures is explored in earlier publications.[2,3] The analysis in these references includes determination of the voltage required on a two-membrane sandwich structure to offset normal compressive orbital perturbations to the structure. The compressive pressures would tend to collapse the membrane structure, thus must be compensated by the inflation pressure. In GEO, solar radiation pressure is the dominant compression pressure of the orbital perturbations. In LEO, solar radiation pressure dominates until an orbit altitude of approximately 500km, under which atmospheric drag becomes the dominant pressure. To offset the normal compressive orbital pressures, it was found that hundreds of volts are required in GEO and a few kilovolts in LEO. Figure 3.3 illustrates a box-like membrane structure overcoming 1-g of gravity to inflated using a few kilovolts in atmospheric laboratory conditions.

Many challenges to the electrostatic inflation concept exist, such as plasma Debye shielding, space weather, orbital perturbations which may tend to collapse the structure, and complex structural dynamics. In the space plasma environment, electrons and ions rearrange to maintain macroscopic neutrality when perturbed by an external electric field.[4] This phenomena causes a steeper dropoff in the potential surrounding a charged object than would occur in a vacuum, thus limiting electrostatic force actuation, especially in cold, dense plasmas. In addition to Debye shielding, the plasma

---

[2] Stiles, L. A., Schaub, H., Maute, K., and Moorer, D. F., “Electrostatic Inflation of Membrane Space Structures,” AAS/AIAA Astrodynamics Specialist Conference, Toronto, Canada, Aug. 2–5 2010, AIAA- 2010-8134.

[3] Stiles, L. A., Schaub, H., and Maute, K. K., “Voltage Requirements for Electrostatic Inflation of Gossamer Space,” AIAA Gossamer Systems Forum, Denver, CO, April 4–7 2011.

[4] Bittencourt, J. A., Fundamentals Of Plasma Physics, Springer-Verlag New York, Inc., 175 Fifth Avenue, New York, NY, 2004.

complicates charging of a spacecraft due to ram effects as a spacecraft moves through the plasma and also wake effects behind the moving craft. For the EIMS concept, it will be important to understand how the charge will flow around the structure and affect inflation. Experiments described within this report were aimed at studying shape stability during charge deflection experiments. Such tests require that the charging experiments are performed in a controlled vacuum chamber with high-quality pumps to avoid issues with ionization of a low-pressure atmosphere. For the experiments discussed in this report, the chamber achieved a vacuum of 10^{-7} Torr for inflation tests and 10^{-6} Torr for charge deflection experiments.

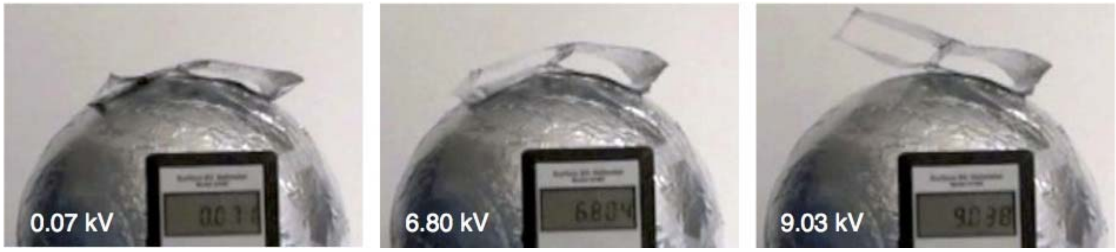

Figure 3.3: Atmospheric Electrostatic Inflation Experiment of a Box-Like Membrane Structure

3.3 Radiation Shielding Background

Radiation shielding is a critical challenge with envisioned manned space exploration activities. The dangers of radiation to biological tissue must be well understood, and protection incorporated into any space travel concept. This is particularly true for long duration missions and travel beyond Low Earth Orbit. Radiation shielding can be accomplished with passive or active methods, or a combination of the two. Current designs employ passive damping where sufficient material is present to absorb enough of the harmful high-energy ion radiation. This concept has the benefit that no active control is required, and thus it provides a robust solution. One drawback of passive shielding is the mass of the materials required for adequate radiation safety. This mass is a challenge when designing interplanetary human explorations. A savings in the mass required to perform radiation shielding would enable significant mission cost reductions.

Use of electrostatic fields is one active method that provides an alternative to bulk material passive shielding.[5] Other forms of active shielding include plasma shields, confined magnetic fields, and unconfined magnetic fields.[6] Some of the challenges of active electrostatic shielding, such as high potentials and size limitations due to electrical

---

[5] Spillantini, P., Casolino, M., Durante, M., Mueller-Mellin, R., Reitz, G., Rossi, L., Shurshakov, V., and Sorbi, M., “Shielding from cosmic radiation for interplanetary missions: Active and passive methods,” Radiation Measurements, Vol. 42, No. 1, 2007, pp. 14 – 23, DOI: 10.1016/j.radmeas.2006.04.028.

[6] Townsend, L., “Overview of active methods for shielding spacecraft from energetic space radiation,” Physica Medica, Vol. 17, 2001, pp. 84–85.

breakdown, have deterred further research on the subject.[7] In Reference 7, Tripathi challenges the claim that electrostatic shielding may be unsuitable and explores a feasible design for radiation shielding, as shown in Figure 3.4.

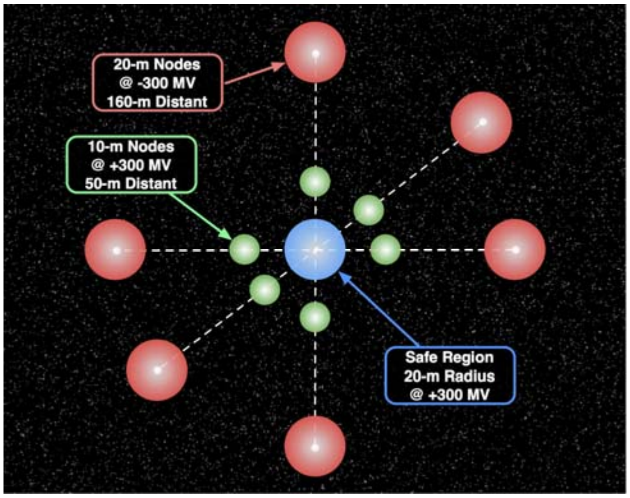

Figure 3.4: Electrostatic space radiation shielding concept

The 10-sphere design requires potentials of 300 MV, and would be used in conjunction with passive material shielding. The author notes that the ability to achieve 300 MV potential levels remains as future work. For EIMS applications, only potentials in the tens of kilovolts have been explored to study the ability to inflate and overcome membrane residual stresses, therefore investigating the feasibility of potentials beyond tens of kilovolts is part of future work. Radiation shielding capabilities of EIMS charged within a range of 0-5 kV are described in the results section of this report.

3.4 Project Scope

This report describes experiments performed as part of NIAC 2011 study conducted at the University of Colorado at Boulder during the performance of NIAC effort. The CU facilities used for the study include a small vacuum chamber that is 30cm in diameter and 60cm long with pressures feasible to the 10^{-7} Torr range. Such a chamber was ideal for cost-effective initial deployment and shape testing of EIMS test concepts and charge bombardment experiments. This vacuum chamber, pumps, and high-voltage interfaces are owned by Dr. Zoltan Sternovsky of the University of Colorado. He is an international expert on dusty plasma physics and high-voltage charge transfer experiments. His help in this effort is greatly appreciated.

---

[7] Tripathi, R. K., Wilson, J. W., and Youngquist, R. C., “Electrostatic space radiation shielding,” Advances in Space Research, Vol. 42, No. 6, 2008, pp. 1043–1049, DOI: 10.1016/j.asr.2007.09.015.

4. Experimental Setup

The setup for the radiation experiments includes an electron gun at one end of a vacuum chamber and a Faraday cup positioned behind a membrane structure at the opposite end of the chamber. The electron gun will emit electrons and the Faraday cup will measure the current, allowing observation of the flow of electrons around an EIMS structure and providing insight into how an EIMS structure can be used for radiation shielding. The EIMS structure is charged with a high voltage power supply system external to the vacuum chamber. The concept is illustrated in Figure 4.1.

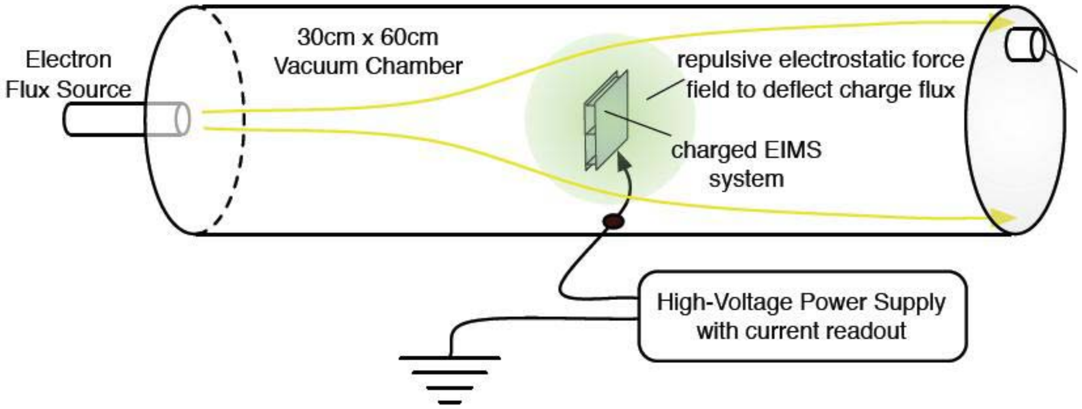

Figure 4.1. Concept illustration for the radiation shielding experimental setup

4.1 High Voltage EIMS Charging Setup

The first component of the experimental hardware that was designed and built was a high voltage EIMS charging setup. The charging setup is used to apply a desired voltage to the membrane structures for inflation.

Figure 4.1 displays a diagram of the setup. The high voltage is supplied by an Ultravolt 40A Series high voltage DC-DC converter. This device supplies up to -40kV to the membrane structures. The voltage magnitude is controlled by a user through a Graphical User Interface on a Macbook computer, as shown in Figure 4.2. A National Instruments USB-6008 data acquisition device is used to drive the power supply and also to record current and voltage data.

This custom software allows the EIMS to be charged to a particular absolute voltage by either manually moving the voltage slider, or by running a predefined voltage history on the structure. For the following experiments that setup is such that the voltage is being held at a fixed value which charge flux and EIMS stability observations are made.

4.2 Charge Deflection Hardware Components

Figure 4.4 illustrates each of the components of the experimental setup. A summary of the setup is as follows: the electron gun is heated and electrons produced by thermionic emission are accelerated from the filament, biased to -5 kV, toward the grid, which is grounded. A membrane structure hangs between the electron gun and a detector to read the current behind and around the structure.

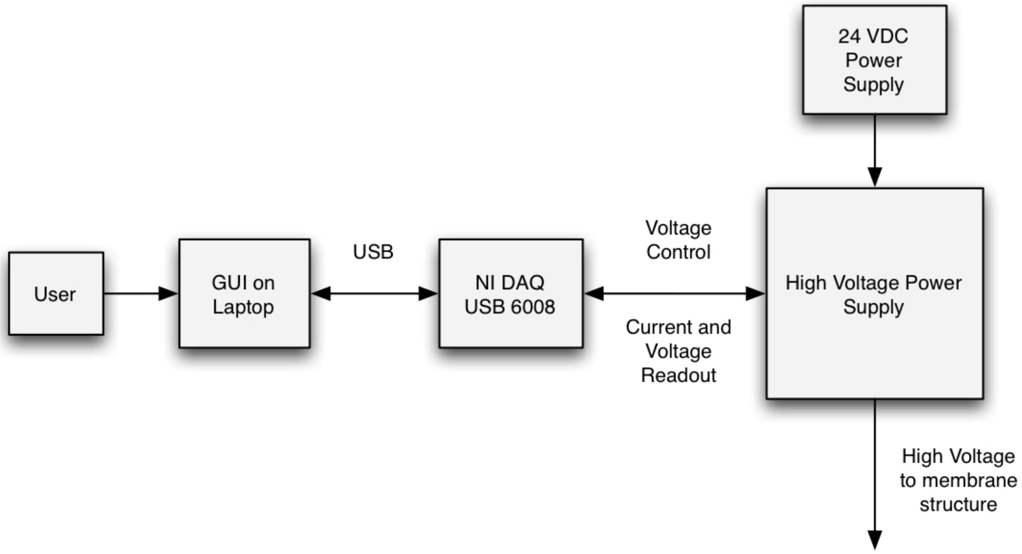

Figure 4.1. Block diagram of high voltage charging setup for membrane structures

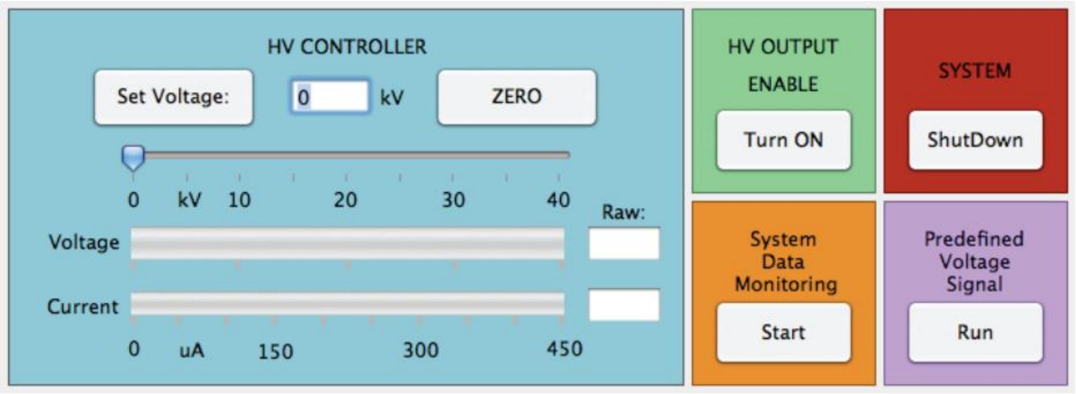

Figure 4.2. Graphical User Interface for operating the high voltage charging setup

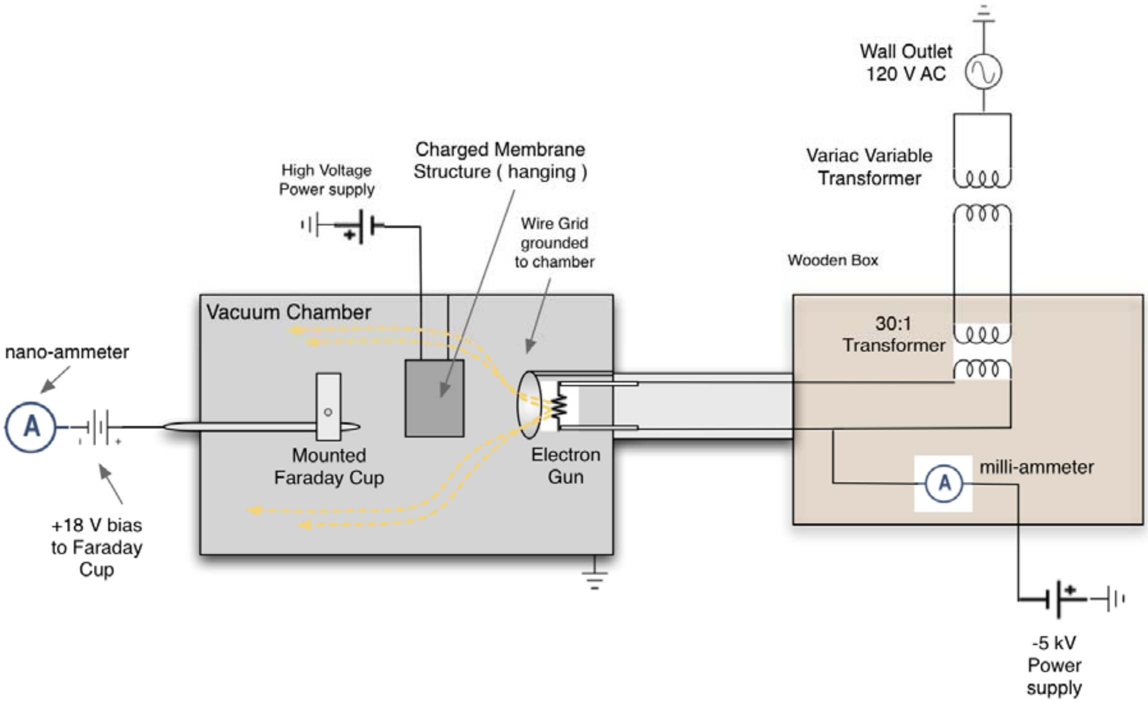

Figure 4.3. Radiation Experiment Hardware Diagram

Figure 4.4 shows the constructed electron emitter. The filament is heated and electrons accelerated off by the electrostatic field between the filament and the grounded wire mesh.

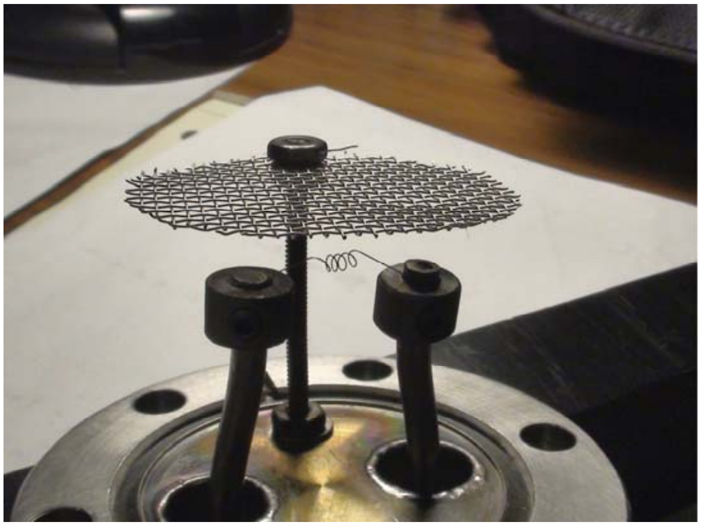

Figure 4.4. Electron gun filament and wire mesh

The filament is constructed of 5mil coiled Tungsten wire. The length of the Tungsten wire was chosen based on the resistivity of the metal, ρ, and the electrical resistance, *R*. The resistivity of Tungsten near the melting point is approximately 10^{-6} Ohm-meters and the electrical resistance was measured in the lab to be 2-3 Ohms. Using the below equation, the 5 mil wire (cross sectional area, A=1.3e-8) could have a length, *l*, of approximately 3.8 cm.

$$l = R\frac{A}{\rho}$$

The current emitted from the tungsten coil can be tuned by changing the setting of the Variac variable transformer. The higher the AC current supplied to the coil, the higher the temperature, thus more electrons can be accelerated toward the grid. The high voltage power supply providing the DC bias to the coil is current-limited at 5 mA, therefore the maximum emission current is 5 mA.

The FC-70 Faraday cup was chosen as the device to detect current inside the chamber. The detector has a small aperture into which electrons can flow to measure the ambient current. The FC-70, shown in Figure 4.5 is mounted onto an aluminum plate with a collar attached with vacuum epoxy. The collar allows for mounting the device onto a rotatable vacuum feedthrough probe. The rotatable probe allows the Faraday cup to sweep through an angular range of approximately 120° thus providing positioning both behind and to each side of the membrane structure.

Figure 4.5 Mounted Faraday cup with collar for attachment to vacuum feedthrough

The output of the Faraday cup is connected to a digital multimeter with DC current resolution to picoAmps. A battery is located in the path between the nano-ammeter and the Faraday cup. The battery is a combination of the two 9 Volt batteries connected in series to bias the Faraday cup by 18 V. This small voltage helps to eliminate low-energy secondary electrons from entering the aperture of the Faraday cup.

5. Electromechanical Vibrations Study

A key research focus of the charge shielding experiments was to explore the cause of small structural vibrations observed during charge bombardment of EIMS. This section describes the nature of the vibrations as well as the experiments to investigate to the cause.

5.1 Vibration Mechanics

The experiments show that the membrane structure is stable, in the sense that it does not collapse or undergo major shape changes, in all of the ranges of particle flows created (up to 5mA emission current and energies up to 5keV). However, small structural vibrations were discovered when the structure is charged and the electron gun is emitting a flow of electrons. To observe the vibrations, the membrane structure must be electrostatically inflated while the electron gun is emitting electrons. No vibrations are present with an uncharged membrane structure in the electron flux.

The vibrations are seen at both very low currents and the currents near the maximum of 5mA. The vibrations, however, are not seen through the full continuous sweep of currents. Rather, at particular charge flux and electrostatically inflationary pressure combinations a resonance-like vibration appears. If the EIMS voltage is changed upwards or downwards, the vibrations can cease until new critical conditions are achieved. Similar patterns are seen for the full range of membrane structure voltages (0 to 10 kV) and electron energies (0 to 5 keV).

Figure 5.1 is shown to convey the magnitude of vibrations in the structure. It is difficult to capture the small oscillations, but a difference can be seen in the membrane shadows of Figure 5.1. The vibrations are of small magnitude and ripple across the membrane structure.

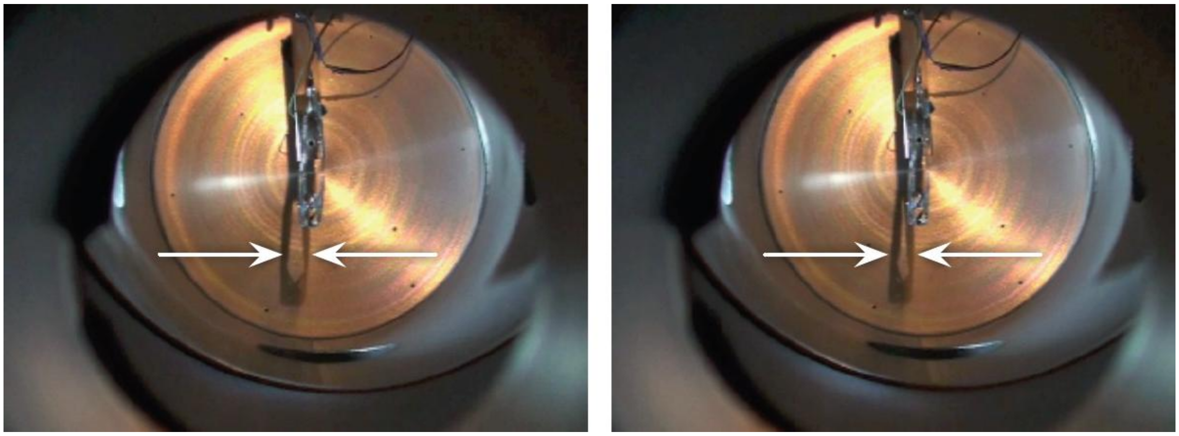

Figure 5.1: Photos of vibrating membrane structure. Vibration amplitude illustrated through shadow

A Strobotac stroboscope was used to investigate the frequency of the vibrations. Often, there were several different vibration frequencies present at a given instant. This indicates a complex ripple of vibrations is present as small shape changes occur, not just a single standing vibration. The primary frequencies measured were around the 4 Hz range. The vibrations experiments were also performed with different membrane structures. One of these structures was constructed from two solid 8 x 10 cm sheets with additional weight at the bottom to tension the structure, as seen in Figure 5.2.

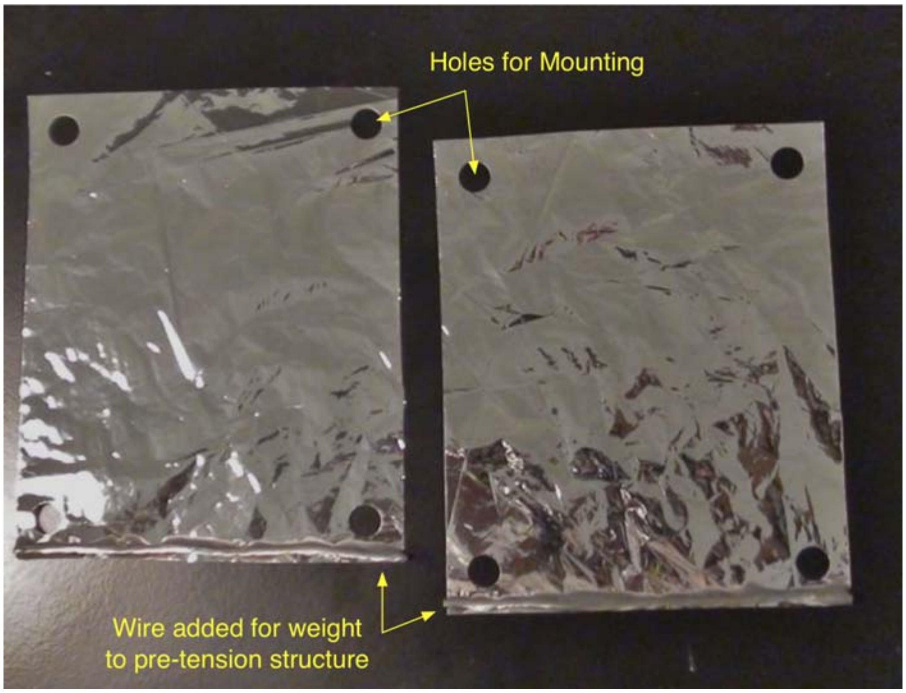

Figure 5.2: Weighted structure for vibrations experiments

The stroboscope was used to determine the approximate frequency of vibrations in the pre-tensioned structure. The vibrations were found to be near 8 Hz, approximately twice the frequency of the previous unweighted structures. The vibrations were also more consistent through the entire membrane.

5.2 Source of Vibrations

Several potential sources of such vibrations were investigated and eliminated. First, it is possible that the deflected charge flux imparts a sufficiently large momentum exchange with EIMS to cause this rippling. To investigate this possible cause, experiments with a single membrane sheet were performed. None of the single-sheet experiments, charged or not charged, showed any visible vibrations, even sweeping through all feasible electron energies and all electron currents. These results suggest that the vibrations are un-likely caused by a transfer of momentum. Otherwise, vibrations or deflections would have been seen with single sheet experiments.

Secondly, the electron flux itself could be a source of these vibrations if the electron gun emitted flux is not steady, but has frequencies near 4Hz. To investigate this possible vibration cause, the electron flow output signal from the emitting gun is studied with an oscilloscope. The Fourier transform function of the oscilloscope is used to determine frequencies present in the driving current signal. The only significant frequencies present were the power line frequency of 60 Hz and a very high frequency in the kiloHertz range. Neither of these frequencies are in the 4Hz range of the observed structure vibrations.

Thirdly, fluctuations in the EIMS external power supply performance could cause EIMS vibrations. In essence, if the actual EIMS voltage is not held steady, but cycles in the presence of the external charge flux, then these voltage variations would directly results in the electrostatic inflation pressure varying. As a result, the EIMS structure would slightly deflate and inflate. An oscilloscope is used to examine the output of the power supply which charges the membrane structure. The power supply has an internal feedback loop to ensure a digitally commanded reference voltage level is maintained. The measure output signal provides a measurement of how well this voltage is being held constant. It was speculated that the power supply may be overcompensating as the external charges from the electron gun change the charge on the structure. It was found, however, that the power supply output frequencies, with and without the EIMS vibrations present, showed no significant difference. In fact, the power supply fluctuations were very small, barely observable, and more than an order of magnitude larger than the observed EIMS vibrations. Thus, it is concluded that the power supply did not provide first order contributions to the EIMS vibrations. Otherwise, output power variations during EIMS vibrations would leave a unique fingerprint.

Finally, the question remains, what is driving these EIMS vibrations under particular electron flux and electrostatic inflation pressure conditions. The hypothesis is that the membrane surface vibration is a result of local surface charge density variations causes by the charge flux. As the charge density, σ, varies, then the local electrostatic inflation also changes. Since the EIMS system is in equilibrium between the 1-g gravitational forces attempting to compress the structure, and the electrostatic pressure inflating the structure, a small change in electrostatic pressure will negate this equilibrium and result in a local shape deformation, outward or inward. This shape change, in return, will cause a change in the surface normal electrostatic field which impact the near-surface charge flux.

Analytical or numerical proof of this hypothesis will require considerable effort to model the time varying flux and structural response. However, thus far, all experimental results support a dynamic coupling between the charge flux and the local charge distribution, resulting in the observed small magnitude vibrations. Further, note that this hypothesis requires the structure shape to be in equilibrium between competing electrostatic pressure and compressing gravity forces. This raises the question if such EIMS vibrations would manifest if the structure were in space without any acceleration present. If the electrostatic pressures are sufficiently large, here the shape inflation is not limited by gravity, but by internal support structure and membrane surface tension. Thus, a loss in pressure will not result in a shape change until the pressure is less than an externally compressing perturbation. In the absence of gravity, a gravity-like perturbation must still be considered if the structure is accelerated through an orbital maneuver. In particular, orbital maneuvers with EIMS are most likely to be performed with fuel-efficient low-thrust technologies. Thus, the future work investigating modeling and predicting such vibration behavior is of great importance.

5.3 Electron Gun Trade Study

A study was performed to evaluate a new design for the electron gun. The current design consists of a tungsten filament and a biased wire mesh to accelerate electrons. One consideration was to purchase a commercial electron gun. Commercial electron guns provide a wide array of options, including various electron energies, emission currents, beam angles, and pulsing capabilities. Several of the low and medium energy options investigated from Kimball Physics would be appropriate devices, yet the price range was beyond the budget of the current research project. Electron gun prices were shared with the sponsor. Commercial options will remain as a possibility in the future for a more controlled, focused electron beam.

Besides commercial options, modifications to the current electron gun were considered. In particular, deflection plates for the electron gun would aid in focusing the beam of electrons. This idea is similar to a cathode ray tube, as seen in Figure 5.3[8], where deflection plates are used to control the direction of the stream of electrons with an electrostatic field.

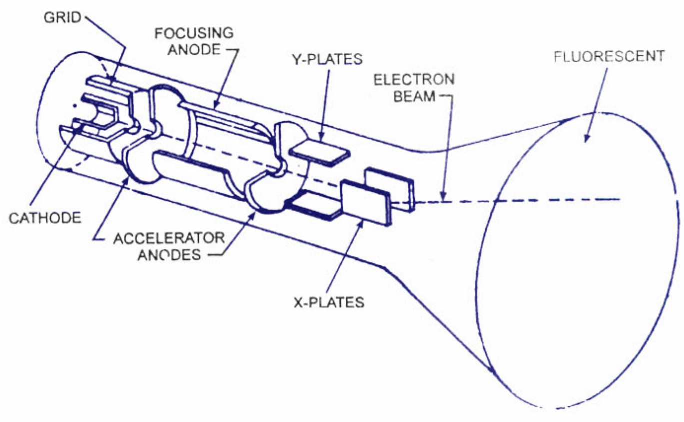

Figure 5.3: Cathode Ray Tube schematic showing deflection plates used to control the path of electrons

Another similar option is a biased ring or disc through which the electrons would pass to refine the spray of the electron gun into a more directed stream. Due to the geometry of the current electron gun, any modification would involve a complete rebuild of the device. However, at this stage of the research such enhancements were found not to be necessary. As will be seen in the later section, the University of Colorado was able to obtain good three-dimensional charge wake measurements about EIMS in the test chamber. Future work with a more focused charge emission will allow for edge and slot charge wake effects to be experimentally studied that were beyond the scope of this small study.

---

[8] http://www.circuitstoday.com/crt-cathode-ray-tube

6. Extended Charge Deflection Experiments

Experiments with a charged structure in the electron stream were performed to understand the charge flow patterns around the electrostatically inflated membranes and also to study the charge deflection capability of low energy electrons. A Faraday cup position is rotated within the chamber to obtain a sweep of charge flux measurements down-stream of the EIMS. The probe on which the detector is mounted allows for rotation through approximately 120 degrees. Further, the probe can be positioned at different distances behind the EIMS. This allows for a three-dimensional measurement to be taken to study the mean charge wake behavior down-stream of the EIMS. Measurements of detected current are recorded as the probe and detector are swept through the physically feasible angular range. The rotation of the detector is illustrated in Figure 6.1. 3D surface plots are used here to represent the data from these experiments.

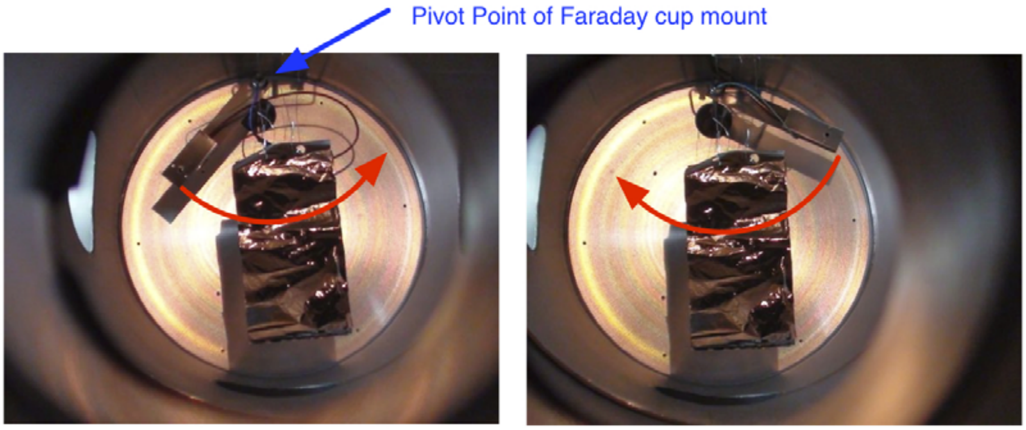

Figure 6.1: Rotation of the Faraday cup around the membrane structure

The first experiments were performed without a membrane structure in the vacuum chamber. The setup without a membrane structure allowed for determining a baseline of the natural charge flow patterns within the chamber. A 3D surface plot with the data collected with no structure is shown in Figure 6.2. The charge drop-off with increased distance from the electron gun is seen, as well as a variation as the detector is rotated from one side of the chamber to the other side.

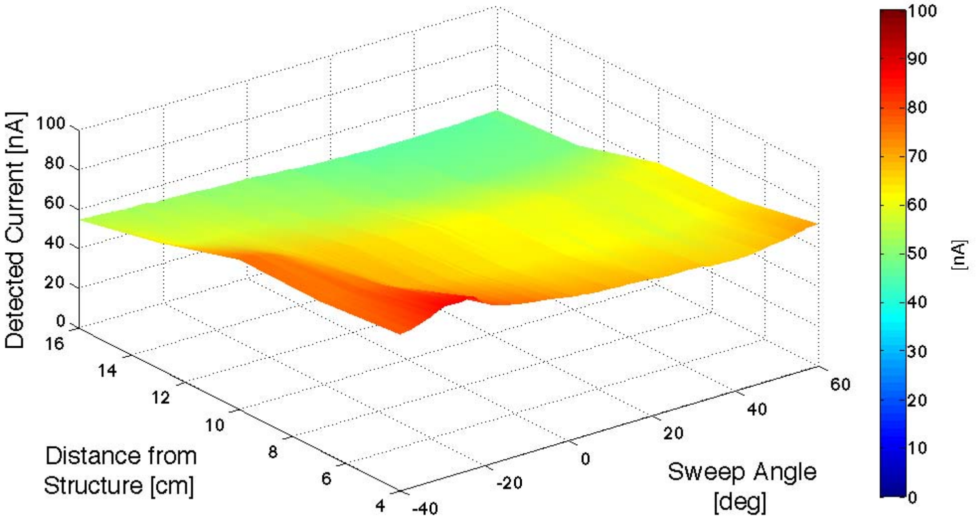

Figure 6.2: Electron flux with no membrane structure present (baseline flux)

Next, in Figure 6.3 the uncharged EIMS is added to the chamber, and subjected to a similar charge flux. The multi-micron thick aluminum coated Mylar is too thick for the 5keV electrons to penetrate. Thus, this result illustrates how much of the charge flux blocking is simply due to an uncharged EIMS. The electron flux directly behind the structure (approximately -20 to +15 degrees) drops from the 70 nA range down to the 25 nA range.

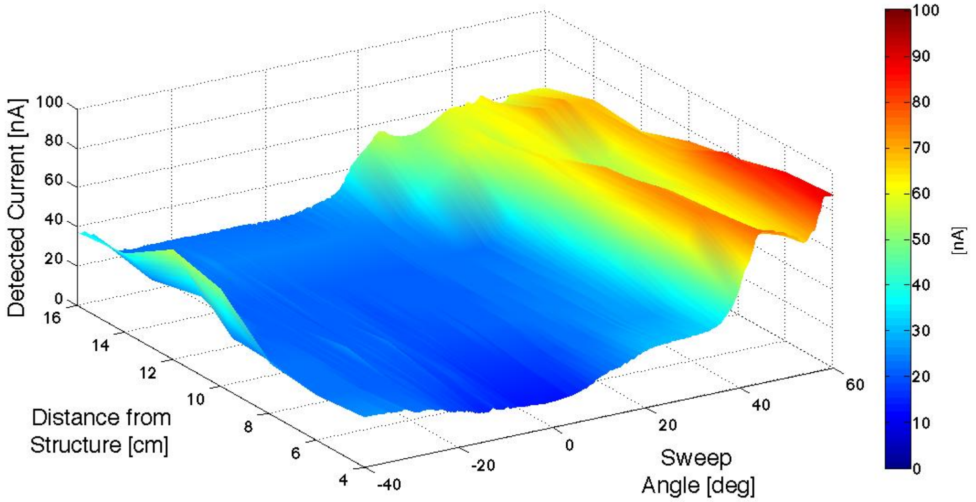

Figure 6.3: Electron Flux behind charged and uncharged EIMS of size 8 x 10cm

Next, the same data collection was performed with a charged structure at 4kV and 8kV. These two voltages were chosen such that one voltage was below the energy of the electron gun (5 keV) and one above. The surface plots are shown in Figure 6.4 for the 4 kV charging level and in Figure 6.5 for 8kV charging level.

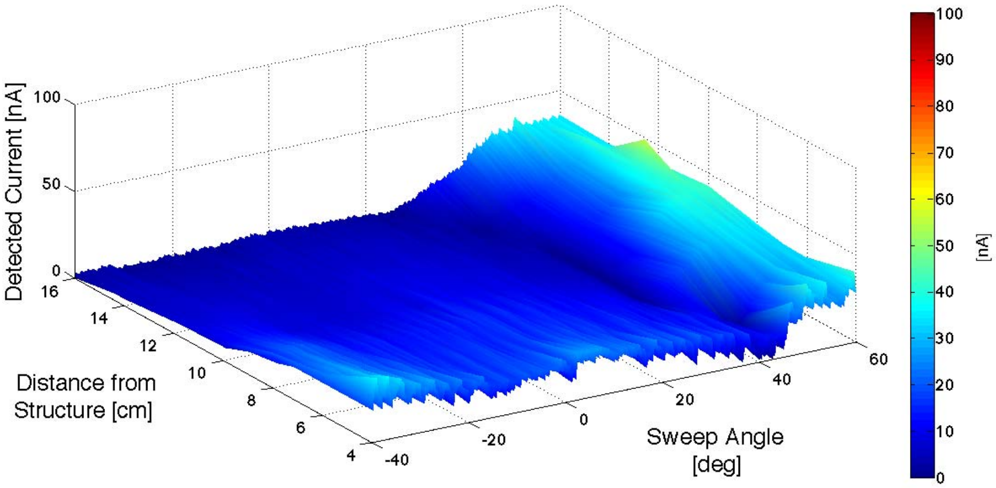

Figure 6.4: Electron Flux behind charged and EIMS of size 8 x 10cm charged to 4 kV (below electron energy)

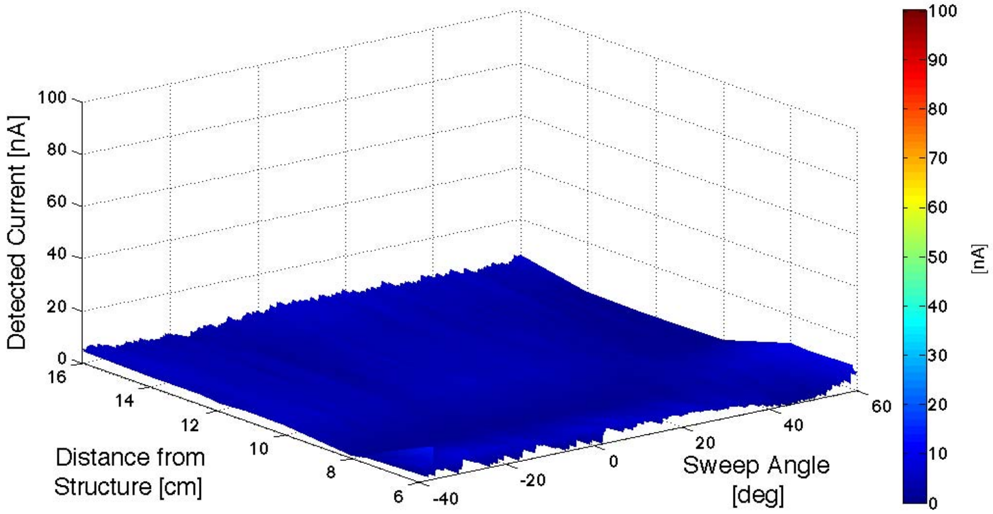

Figure 6.5: Electron Flux behind charged and EIMS of size 8 x 10cm charged to 8 kV (below electron energy)

When the structure is at 4kV and below the electron energy, there is still current in the 20 nA range behind the structure. There is an overall drop, however, in the amount of current detected anywhere behind or to the side of the structure. When the structure is charged to 8kV, there is another big drop in the current levels detected. All recorded currents are below 12 nA and are in the single digit nA range behind the structure. These plots clearly show the low-energy electron shielding capabilities of a charged membrane structure.

7. Membrane Materials Study

A brief study of membrane materials was performed as a part of this project. In experiments prior to this project, EIMS had utilized only one membrane material: ¾ mil aluminized Mylar. Here, thinner materials are considered to observe and compare inflation capabilities and vibration mechanics.

7.1 Materials

Samples of two new materials were obtained for this project: $^1/_4$ mil Aluminized Mylar and $^1/_3$ mil Aluminized Kapton. These thinner materials have presented challenges in preparation for the vacuum chamber. The Aluminized Kapton material begins to warp after a prolonged period in the ethanol sonic bath, thus required development of new cleaning procedures. A photo of the warped membrane is shown in Figure 7.1.

Figure 7.1: Warped membrane following ethanol sonic bath

Another membrane issue that was encountered with the thinner materials is melting at the point of contact with the charging wire. This was observed with the $^1/_4$ mil Aluminized Mylar and is shown in Figure 7.2. This is likely due to the high current when rapidly charging the membrane structures. This melting was never encountered with the $^3/_4$ mil Aluminized Mylar. When using these thinner materials in the future, slower charging may be required to avoid high currents that may melt the material. This important result illustrates that charging currents must be considered when designing electrostatic charge deflection surface. While the membranes provide a novel light-weight solution, their thin conducting coating can provide increased electrical resistance when attempting to impart charge with a power supply. If the current is too large, i.e. the voltage change is rapid as experimentally performed with these thin membrane materials, the heating is sufficient to plastically deform and damage the membranes. Thus, while electrostatic inflation with the lighter membrane materials were possible, additional thermal considerations must be considered.

Figure 7.2. Melted membrane from contact with charging wire

7.2 Experiments

Inflation tests were performed in a vacuum environment with the $^1/_4$ mil Aluminized Mylar. Figure 7.3 shows the new structure inflated to 8 kV in the vacuum chamber.

Figure 7.3: The $^1/_4$ mil membrane structure inflated in the vacuum chamber

The thin structure inflated with slightly lower voltages than those required for full inflation of the thicker, $^3/_4$ mil material structure. Other factors, however, such as vacuum preparation techniques, were required to change for the thinner material structure. The cause for less required voltage, therefore, cannot definitively be definitely attributed to the thinner material. However, at this stage of the research the increased inflation capability is in line with the expected behavior of having a lighter, more flexible membrane.

8. Shape Investigations

Two studies were performed related to the membrane structure shape. First, an analytical development is presented which describes voltage requirements for an electrostatically inflated sphere and also tolerable accelerations of the sphere. Second, numerical electrostatic simulations are presented which were performed to understand the mechanics behind inflation of the membrane structures used in experiments.

8.1 Analytical Development for a Sphere

A study was performed to understand the voltage requirements for an electrostatically inflated sphere to offset orbital perturbation that may tend to collapse the structure. The mathematical development is as follows.

The electrostatic potential energy of the charges on the sphere is described by:

$$U = \frac{1}{2}\int V\sigma dS = \frac{1}{2}VQ$$

As the spacecraft potential is the parameter that is controlled, this can be rewritten as:

$$U = \frac{1}{2}CV^2 = 2\pi\epsilon_0 V^2 R$$

To find the force, we use the derivative of the potential energy:

$$F = \frac{dU}{dR} = 2\pi\epsilon_0 V^2$$

This is the total force acting on the sphere, but we are interested in pressure. The surface pressure would be:

$$P = \frac{F}{A} = \frac{F}{4\pi R^2} = \frac{\epsilon_0 V^2}{2R^2}$$

Figure 8.1 shows the relationship between voltage on the sphere and the pressure on the surface for sphere with a 1-meter diameter.

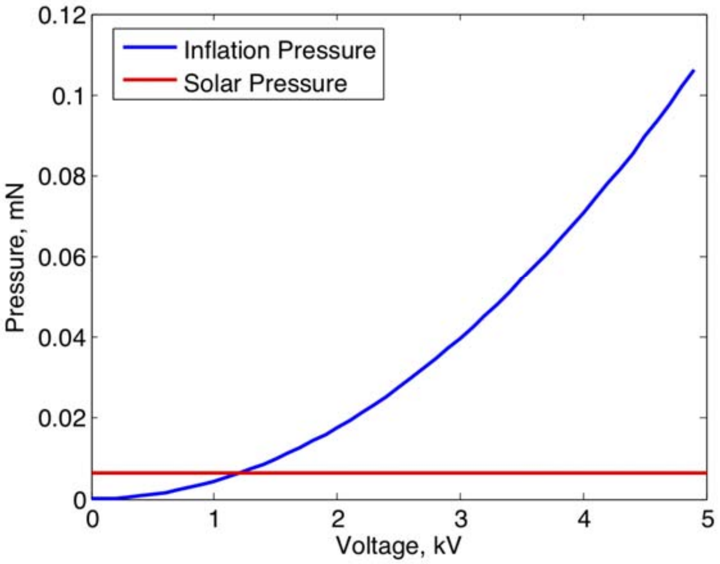

Figure 8.1: Electrostatic pressure and voltage relationship

For GEO, solar radiation pressure is the largest orbital perturbation. This has a constant value of approximately 6.4 μN/m^2 and is shown as a line on Figure 8.1. As seen on the plot, the required sphere voltage to offset this compressive solar pressure is approximately 1.2 kV.

Examining the required pressure to offset solar radiation pressure across a range of sphere radii, it is seen that the required voltage remains feasible up to large craft sizes of 30 m radii. This is shown in Figure 8.2.

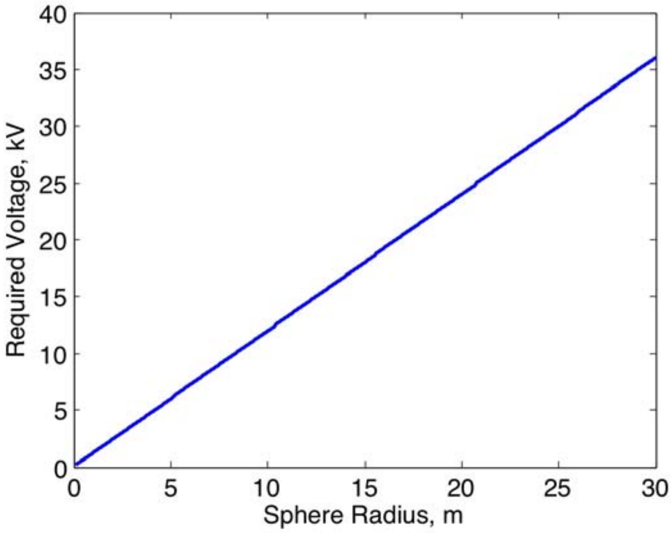

Figure 8.2: Voltage to offset solar radiation pressure for a range of sphere sizes

Similarly, a study was performed to understand the level of acceleration that an inflated sphere can withstand before beginning to collapse. Using a simple spring mass model of the inflated structure, a range of sphere radii and sphere voltages were studied. The results are shown in Figure 8.3. Higher voltages allow greater accelerations whereas larger radii limit the acceleration.

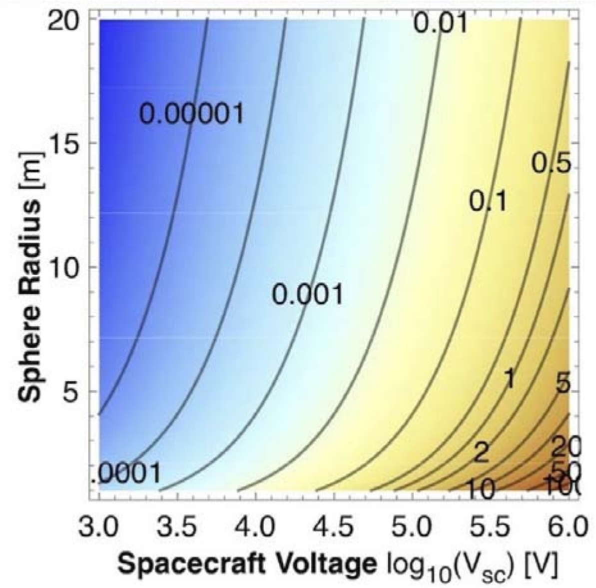

Figure 8.3: Allowable G-forces for an inflatable sphere

8.2 Electrostatic Numerical Simulations

To numerically study the electrostatic characteristics of different membrane shapes, the 3D electrostatic solver software `Maxwell 3D' was utilized. Maxwell 3D allows simulation of the electrostatic forces and fields, capacitance, and charge distributions of user-defined geometries. The study performed was to investigate the electrostatic benefits of the membrane material cut-outs in the structures which inflate well in the laboratory and vacuum environment. Figure 8.4 shows the geometry of the cut-out structures and Figure 8.5 shows a solid membrane, each showing the electrostatic charge distribution given the same applied voltage. Notice in Figure 8.5 the increased charge distribution in the region of the membrane cut-outs. The magnitude of the charge distribution at these edges is nearly a 40% improvement of the charge distribution in the same location of the solid membrane. This increased charge yields a larger electrostatic force and therefore, a greater inflation pressure. Further, a non-solid membrane concept will enable further mass savings.

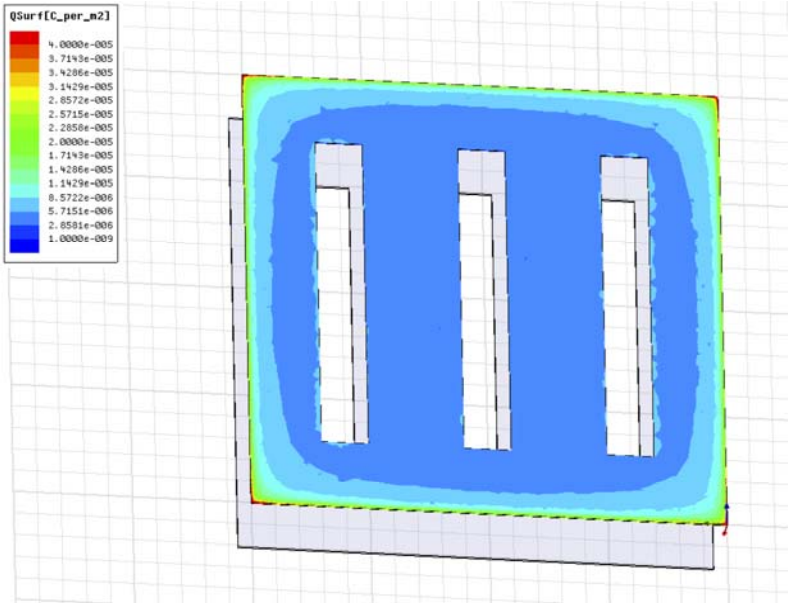

Figure 8.4: Charge distribution from electrostatic simulation of cut-out membrane structure

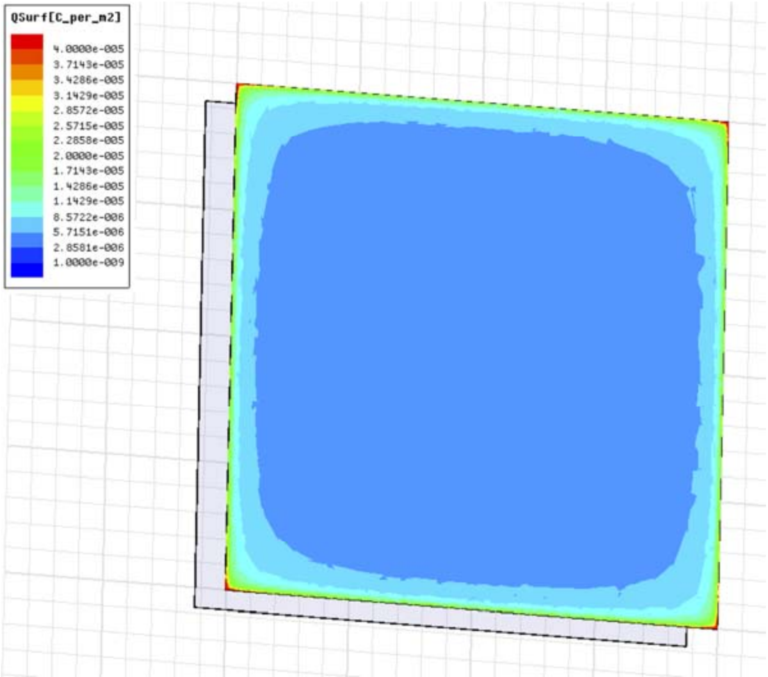

Figure 8.5. Charge distribution from electrostatic simulation of solid membrane structure

9. Power Requirement Study

The question of power requirement is a serious consideration for active space radiation shielding systems, including the electrostatic deflection scheme considered in this study. Thus, to supplement the electrostatic charge deflection experiments, a simplified analytical power assessment was performed to provide an approximation as to the order of magnitude of power required to maintain fixed voltage in a variety of representative plasma conditions. To obtain preliminary estimates of expected power levels, the power required to maintain a single sphere in a space plasma environment with a photo-electron current is considered. The charged spheres will create complex charge wake behaviors which impact the individual power needs of a multi-sphere setup. Such level of detail is well beyond the current scope of this project. Rather, the single-sphere power study illustrates if the low-energy, nominal space environment dominates the power evaluation, or if the high energy solar and galactic particles must be considered as well.

Section 0 provides an assessment of the nominal power requirement for maintaining a fixed electrostatic potential within the ambient deep space plasma environment. Sections 0 and 0 quantify the power impact incurred by typical solar particle events (SPE) and galactic cosmic radiation (GCR), and Section 0 offers an outlook as to the challenge of developing an electrostatic radiation shielding scheme that is robust *and* power-efficient.

9.1 Nominal Power Requirement

Preliminary power computations were performed to evaluate the practicality of maintaining a fixed potential within plasma conditions representative of deep space. Currents incurred by local ion and electron densities and the photoelectric effect are incorporated in these analytical power estimates; secondary emissions and backscattered electrons are neglected. For an isolated EIMS node with a 10-meter radius and active charge control device, the net plasma current flow is approximated as:

$$I_{net} = I_e - I_i - I_{Pe} \pm I_{cc}$$

where I_e and I_i denote currents generated by the ambient electron and ion populations, respectively, I_{Pe} is the current due to photoelectric scattering, and I_{cc} is the charge control current. To maintain a fixed spherical EIMS potential, the charge control device is employed to drive $I_{net} = 0$, such that I_{cc} is given by:

$$I_{cc} = I_e - I_i - I_{Pe}$$

Assuming that the ambient plasma is comprised of electron and proton populations modeled with single-Maxwellian distributions, total electron and proton currents are developed for positively and negatively-charged EIMS with Mott-Smith and Langmuir attraction and Boltzmann repulsion:[9]

$$(I_e - I_i)|_{V_{sc} < 0} = J_{0e} A_n \exp\left[\frac{-e_c|V_{sc}|}{\kappa T_e}\right] - J_{0i} A_n \left(1 + \frac{e_c|V_{sc}|}{\kappa T_i}\right)$$

---

[9] Lai, Shu T. *Fundamentals of Spacecraft Charging: Spacecraft Interactions with Space Plasmas.* Princeton: Princeton University Press, 2012.

$$(I_e - I_i)|_{V_{sc} > 0} = J_{0e} A_n \left(1 + \frac{e_c V_{sc}}{\kappa T_e}\right) - J_{0i} A_n \exp\left[\frac{-e_c V_{sc}}{\kappa T_i}\right]$$

where $A_n \equiv 4\pi R_n^2$ is the surface area of the spherical node, $e_c \approx 1.6022 \times 10^{-19}$ C is the elementary charge, $\kappa \approx 1.3807 \times 10^{-23}$ J/K is the Boltzmann constant, T_e and T_i [K] are the local electron and proton temperatures, respectively, and J_{0e} and J_{0i} [A/m^2] denote the saturation currents at $V_{sc} = 0$:[10]

$$J_{0e} = e_c n_e \sqrt{\frac{T_e'}{2\pi m_e}}$$

$$J_{0i} = e_c n_i \sqrt{\frac{T_i'}{2\pi m_i}}$$

where n_e and n_i are the single-Maxwellian electron and proton particle densities [cm^{-3}] (assumed to be equivalent in this study), $T_{e,i}' = T_{e,i}/\kappa$ are local electron and proton particle energies [J] (also assumed equivalent), and m_e and m_i represent the electron and proton particle masses [kg]. The photoelectric current is an important contributor to current flow for a sunlit EIMS node, and is modeled as:

$$(-I_{Pe})|_{V_{sc} < 0} = -J_{0Pe}\left(\frac{A_n}{2}\right)$$

$$(-I_{Pe})|_{V_{sc} > 0} = -J_{0Pe}\left(\frac{A_n}{2}\right)\exp\left[\frac{-e_c V_{sc}}{\kappa T_{Pe}}\right]\left(1 + \frac{e_c V_{sc}}{\kappa T_{Pe}}\right)$$

where $J_{0Pe} = 20\ \mu$A/m^2 is the saturation current density and T_{Pe} is the photoelectron temperature [K] (derived from mean photoelectron energy $T_{e,i}' = 2$ eV), chosen to represent typical spacecraft materials and provide a conservative estimate of the effect of photoelectric currents on EIMS power requirements. The term $A_n/2$ emphasizes that this current is computed with the sunlit hemisphere of the node only (ambient electron and proton currents are computed with the entire surface area). The power required to maintain a fixed EIMS potential is therefore computed with the expression:

$$P_{req} = |I_{cc} V_{sc}|$$

The EIMS power requirement becomes increasingly more challenging as the spacecraft voltage is increased.

9.2 SPE Power Requirement

For the power requirements investigated in this study, it is of interest to assess the effects of double-Maxwellian plasma distributions developed simultaneous interaction with the ambient plasma environment and that of a solar particle event (SPE). A representative SPE occurred in February 1956 and is summarized in Webber[11], from

---

[10] Hastings, Daniel, and Henry Garrett. *Spacecraft-Environment Interactions.* Cambridge: Cambridge University Press, 1996.

[11] Webber, W.R., "An Evaluation of the Radiation Hazard Due to Solar Particle Events," Boeing Report D2-90469, AeroSpace Division, The Boeing Company, 1963.

which the 1956 Webber differential [particles/cm^2/MeV] and integral [particles/cm^2] SPE spectrum is derived:

$$\frac{d\phi}{dE} = 10^7\left(\frac{E + 938}{\sqrt{E(E + 1876)}}\right)\exp\left\{\left[239.1 - \sqrt{E(E + 1876)}\right]/100\right\}$$

$$\phi = 10^9\exp\left\{\left[239.1 - \sqrt{E(E + 1876)}\right]/100\right\}$$

where E denotes particle energy in MeV. This Webber spectrum is exclusively a proton spectrum and is shown in Figure 9.. Proton densities are required to evaluate the total current, and corresponding power requirements, of an isolated sphere within a double-Maxwellian plasma. Using the integral spectrum fluence data provided in Figure 9., the associated proton density spectrum is determined with:

$$n_p(E) = \frac{\phi}{\tau v}$$

where ϕ is the particle fluence, τ is the reference integration time, and $v = \sqrt{2E/m_p}$ is the velocity. For the February 1956 SPE, the reference time τ is given as 36 hours for particles with $E >$ 30 MeV, and as 19 hours for particles with $E >$ 100 MeV (reference time is computed as the sum of the SPE onset/rise and decay times provided in Reference 11). The proton density spectrum is computed and depicted in Figure 9.2. Only the portion of the integral Webber spectrum in Figure 9.3 satisfying $E >$ 30 MeV is illustrated in Figure 9.2; reference times for less-energetic particles are not provided. Figure 9.2 indicates that for the range of representative SPE energies considered, the higher-energy constituents of the 1956 Webber proton spectrum will not have a strong influence upon the power requirements evaluated for this study. The densities associated with the high-energy particles is orders of magnitude lower than the low-energy particles. While these high-energy particles can be harmful to humans, they have a negligible impact on the electrostatic power requirement. Rather, the low-energy nominal space plasma conditions will dominate the power evaluations.

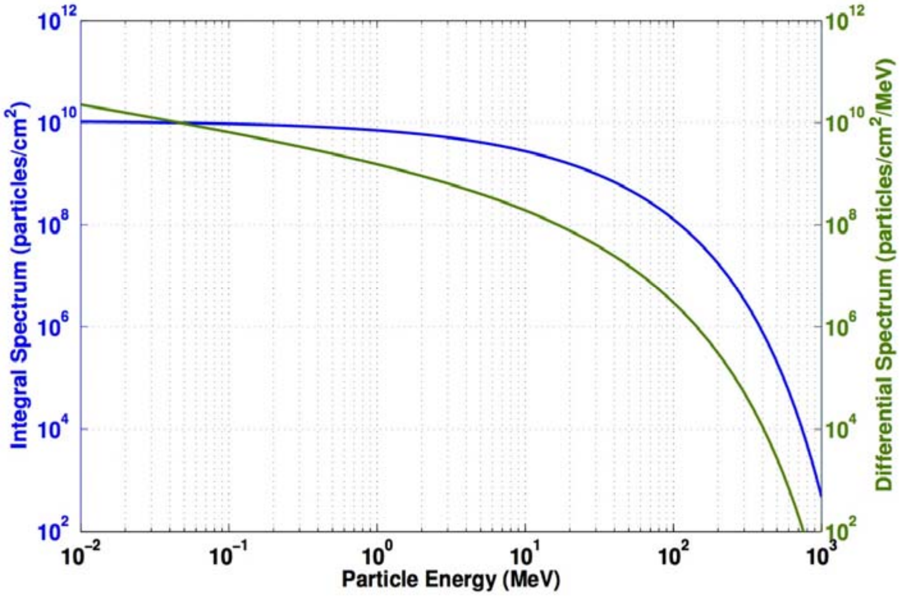

Figure 9.1: The February 1956 integral and differential SPE spectrum

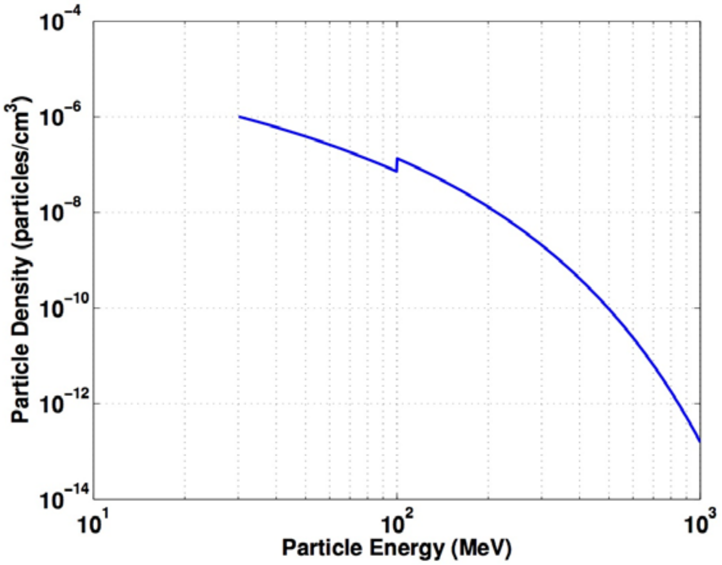

Figure 9.2: Proton density spectrum $n_p(E)$ for 1956 Webber

Employing a Langmuir attraction and Boltzmann repulsion model equivalent to that used to evaluate the nominal power magnitude, the power requirement for maintaining a fixed potential during a nominal SPE is therefore assessed. Figure 9.3 depicts this power requirement for a representative range of potential levels and proton energies. As illustrated, low SPE densities incur a power cost in the sub-Watt regime (nominally beneath the mW level for the majority of the parameter space). SPE thus do not affect the nominal power level required for an electrostatic radiation shielding system.

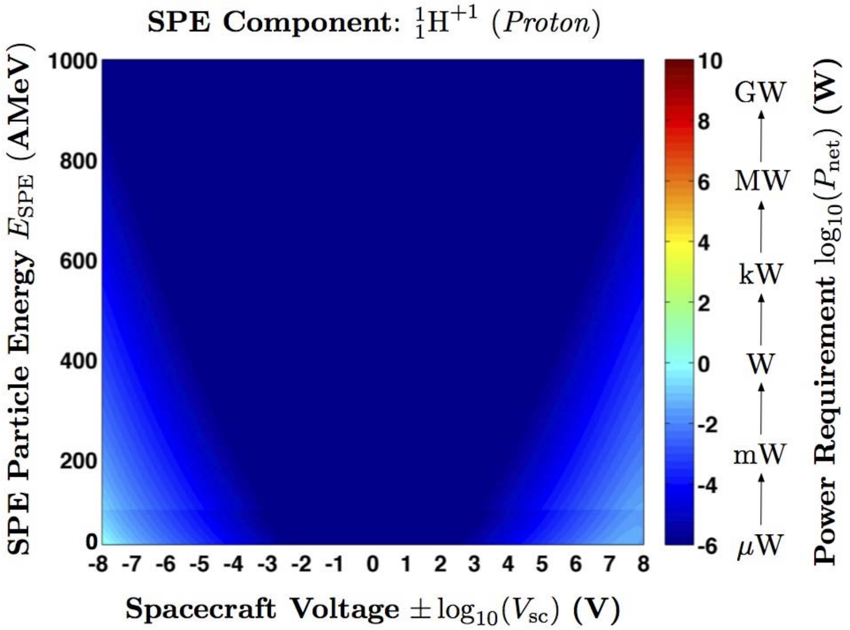

Figure 9.3: Contribution of nominal solar particle event to power requirement

9.3 GCR Power Requirement

To evaluate the effect of high-energy galactic cosmic radiation (GCR) on the nominal power requirement, a data file provided by NASA/Langley Research Center was similarly analyzed. Particle fluences for a variety of ions were converted into densities required for assessing the GCR power impact. As protons and alpha particles (helium nuclei) dominated this fluence data, only these two constituents were included in this power study. Therefore, implementing the Langmuir attraction and Boltzmann repulsion model, the GCR power requirement for a range of potential levels and particle energies was computed, and is shown in Figure 9.4.

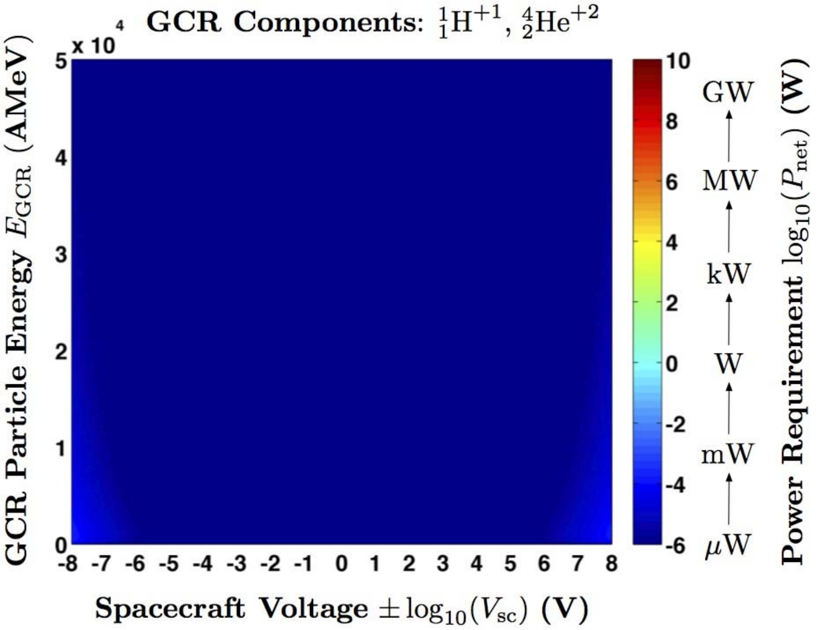

Figure 9.4: Contribution of nominal galactic cosmic radiation to power level

As indicated, the low densities associated with the representative range of particle energies incur a power cost beneath the mW level. As this order of power magnitude is effectively negligible, GCR do not affect the nominal power level required for an electrostatic shielding system. Though the high energies associated with GCR are damaging to human tissue and are thus threatening from a human factors viewpoint, the low densities associated with such energies ensure that the power requirement is insignificant.

9.4 Outlook

The challenges of designing a robust, yet power-efficient node configuration for active radiation shielding are illustrated in Figure 9.5 for a nominal deep-space solar wind energy of 40 eV. These negatively-charged *red* nodes are of 20-m radius and are held at -17 kV; the positively-charged *green* nodes are of 10-m radius and are held at 35 kV. As observed in Figure 9.5, though the positive nodes are charged to a higher potential, they don’t experience any current arising from the plasma influx – therefore, in this situation, the power requirement is driven by the ion currents experienced by the negative nodes on the outside of the deflection configuration, which require active charge control to maintain the desired potential level. The challenge for designing an efficient deflection scheme that is robust to variable space weather conditions lies in the ability to balance node size, position, and potential in an optimal, effective, and power-efficient manner.

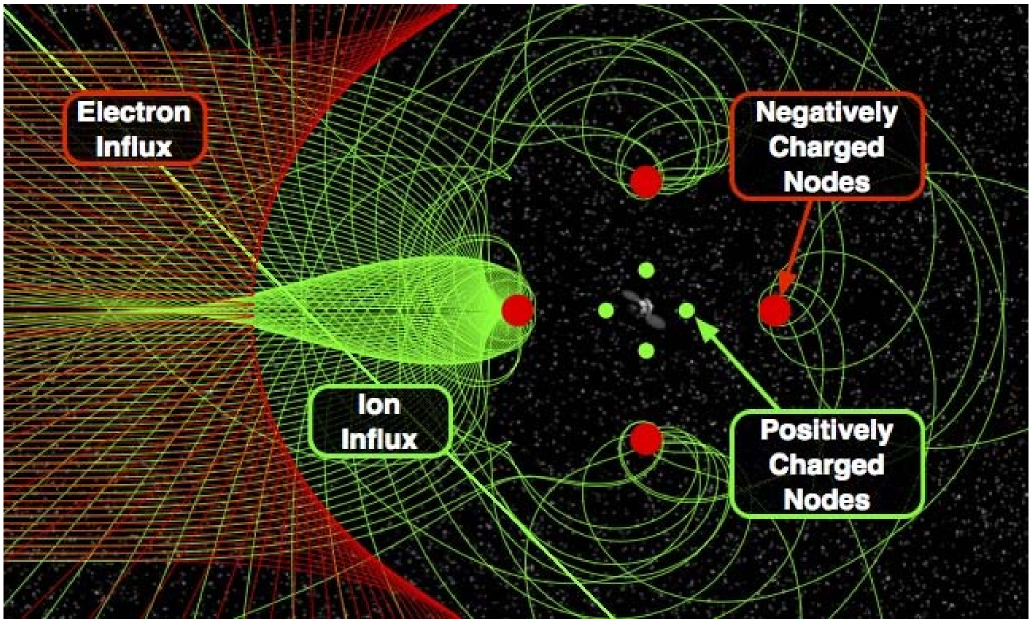

Figure 9.5: Electrostatic deflection for active space radiation shielding with charged nodes

10. NIAC Team

PI - Ram Tripathi – NASA Langley Research Center

Co-I - H. Schaub (Lead Prof.) - Colorado University

Z. Stornovsky, L. Stiles, Paul Anderson, C. Seubert, N. Zinner and J. Mills

Co-I - R. Joshi (Lead Prof.) - Old Dominion University

F. Farrow, H. Qui and A. Mishra

11. Conclusions

This report summarizes research performed on the use of electrostatically inflated membrane structures for active radiation shielding. In this study different innovative configurations were explored to design an optimum active shielding. The study found small membrane vibrations during charge bombardment of an EIMS. Elimination of several potential vibration sources led to the hypothesis that the vibration is a result of local surface charge density variations causes by the charge flux. Within this project, charge deflection and shielding experiments were performed. Plots were presented to describe both the shielding capabilities and the charge deflection patterns around a charged membrane, showing the capability to shield low-energy electrons with EIMS. Also, different membrane materials were investigated, including membrane of much smaller thickness. Too thin materials presented challenges in vacuum preparation and also for rapid charging of membranes. Results from the power requirements study show that the EIMS power requirement becomes increasingly more challenging as the spacecraft voltage is increased. As a result, the emphasis is on the deflection of charges away from the spacecraft rather than totally stopping them. This significantly alleviates the initial power requirements. It was found, though, that SPE and GCR do not affect the nominal power level required for an electrostatic radiation shielding system. During this study electrostatic active radiation shielding technology has significantly been advanced to a much higher maturity and/or TRL level than ever before and has moved a step closer to reality. With modest technological development(s) active shielding is emerging to be a viable option.

12. Acknowledgement

Acknowledgements are due to NIAC Management at NASA Head Quarters for their support and unconditional help and the Program Office at the Langley Research Center, without their generous help the effort would not have been accomplished. It indeed was a joy to work on this project.